Effect of pore fluid on grain-scale interactions and mobility of granular flows: Comparison of distal reach for increasing source volume for dry and and saturated granular flows

Alexander M Taylor-Noonan[1,1], Elisabeth Bowman[2,2], Brian McArdell[3,3], Roland Kaitna[4,4], Jim McElwaine[5,5], and Andy Take[1,1]

[1]Queen's University
[2]University of Sheffield
[3]Swiss Federal Institute for Forest, Snow and Landscape Research WSL
[4]University of Natural Resources and Life Sciences
[5]Durham University

November 30, 2022

Abstract

The presence of a pore fluid is recognized to significantly increase the mobility of saturated over dry granular flows. However, experimental studies in which both the bulk-scale (runout) and grain-scale behaviour of identical granular material in a dry and saturated initial state are directly compared are rare. Further, the mechanisms through which pore fluid increases mobility may not be captured in experimental flows of small volume typical of laboratory conditions. Here we present the results of dry and initially fluid saturated or 'wet' experimental flows in a large laboratory flume for five source volumes of 0.2 to cubic metre. Our results demonstrate that the striking differences in the nature of interactions at the particle scale between wet and dry flows can be directly linked to macro-scale behaviour: in particular, a greatly increased mobility for wet granular flows compared to dry, and a significant influence of scale as controlled by source volume. This dataset provides valuable test scenarios to explore the fundamental mechanisms through which the presence of a pore fluid increases flow mobility by first constraining the frictional properties of the material (dry experiments), permitting an independent evaluation of the implementation of interstitial fluid effects in numerical runout models (wet experiments).

Influence of pore fluid on grain-scale interactions and mobility of granular flows of differing volume

Alexander M. Taylor-Noonan[1], Elisabeth T. Bowman[2], Brian W. McArdell[3], Roland Kaitna[4], Jim N. McElwaine[5], W. Andy Take[6]

[1]Ph.D. Graduate, Department of Civil Engineering, Queen's University at Kingston, Canada (ORCID 0000-0002-5590-7350)
[2]Reader, Department of Civil Engineering, University of Sheffield, United Kingdom (ORCID 0000-0001-7868-6688)
[3]Geologist, Swiss Federal Institute for Forest, Snow and Landscape Research (WSL), Switzerland (ORCID 0000-0002-5322-8741)
[4]Associate Professor, Institute of Mountain Risk Engineering (IAN-BOKU), University of Natural Resources and Life Sciences, Vienna, Austria (ORCID 0000-0002-2289-723X)
[5]Professor of Geohazards, Department of Earth Sciences, Durham University, United Kingdom (ORCID 0000-0002-6292-2014)
[6]Professor & Canada Research Chair in Geotechnical Engineering, Department of Civil Engineering, Queen's University at Kingston, Canada (ORCID 0000-0002-8634-1919)

Key Points:

- Dry granular flows of five volumes between 0.2 to 1.0 m^3 observed to yield a constant travel angle in flume tests
- Saturated flows of the same granular material exhibited a nonlinear decrease in travel angle with increasing volume
- Results provide unique test scenario for simulations by constraining friction properties prior to exploring pore fluid effects

Corresponding author: W. Andy Take, `Andy.Take@queensu.ca`

Abstract

The presence of a pore fluid is recognized to significantly increase the mobility of saturated over dry granular flows. However, experimental studies in which both the bulk-scale (runout) and grain-scale behaviour of identical granular material in a dry and saturated initial state are directly compared are rare. Further, the mechanisms through which pore fluid increases mobility may not be captured in experimental flows of small volume typical of laboratory conditions. Here we present the results of dry and initially fluid saturated or "wet" experimental flows in a large laboratory flume for five source volumes of 0.2 to 1.0 m^3. Our results demonstrate that the striking differences in the nature of interactions at the particle scale between wet and dry flows can be directly linked to macro-scale behaviour: in particular, a greatly increased mobility for wet granular flows compared to dry, and a significant influence of scale as controlled by source volume. This dataset provides valuable test scenarios to explore the fundamental mechanisms through which the presence of a pore fluid increases flow mobility by first constraining the frictional properties of the material (dry experiments), permitting an independent evaluation of the implementation of interstitial fluid effects in numerical runout models (wet experiments).

Plain Language Summary

An accurate prediction of how fast and how far a landslide, such as a debris flow, will travel is essential to define the hazard posed to life and property by these geophysical flows. While dry frictional flows often behave according to the simple physics of friction resisting motion, water saturated granular flows tend to travel farther and faster than the same scenario under dry conditions. In this paper we explore this phenomenon in detail, using high-speed video analysis to look for and quantify differences in grain-scale behaviour that might lead to increased mobility in saturated over dry flows, and high definition laser scans to quantify how far the debris travelled. Large flume tests comparing dry versus saturated flows for five source volumes of 0.2 to 1.0 cubic metres reveal that, in contrast to dry flows, saturated flows travel significantly farther as the volume of the landslide increases. This data is unique as it will enable researchers to test how well numerical simulations are able to model the travel behaviour of the same material in a dry and water saturated state.

1 Introduction

The quantification of the hazard posed by a potential landslide source volume requires an accurate prediction of the travel path and distal reach of the debris. This is generally accomplished in practice by using runout observations from past landslide events in the same location or similar geologic materials to delineate potential hazard areas for future landslides. These observations are then used either within an empirical-statistical approach to define runout exceedance probability (Legros, 2002) or by inferring debris rheological models and parameters from numerical simulations to match runout and inundation depth trimlines of historical events (McDougall, 2017). Heim's Ratio (H/L) was an early empirical-statistical proposal of a parameter for risk assessment by geometrical similarity (Figure 1). The total runout length L has the components of translation of the centre of mass L_{COM} and spreading of the material ahead of the centre-of-mass S_f (Dade & Huppert, 1998; Staron & Lajeunesse, 2009), while the difference in elevation, H, is measured from the back of the head scarp to the front of the debris. The total runout length L is typically of greatest interest for hazard assessment whereas the potential energy of the source volume is often equated to H. As a further development to Heim's Ratio, Parez & Aharonov (2015) then presented a functional model in which the contribution of spreading of the material is related to channel geometry as well as the surface angle of the final deposit.

The travel angle $\alpha_g = \arctan\left(H_{COM}/L_{COM}\right)$ is defined as the angle of inclination between the centre of mass of the runout deposit and the centre of mass of the source vol-

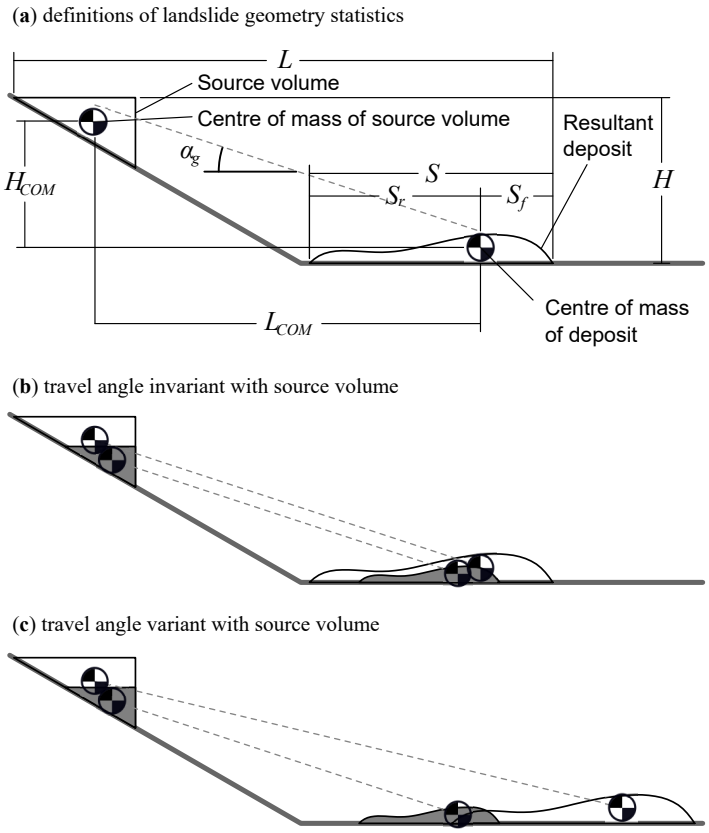

Figure 1. Schematic illustration of flows in a simple planar flume, showing (**a**) definition of geometry statistics, (**b**) the case where the travel angle α_g is invariant with source volume, and (**c**) potential variation of α_g with changing source volume indicating a variation within the rheology.

ume and has been associated with an apparent friction coefficient (e.g. Parez & Aharonov, 2015). Conceptually, the travel angle may be invariant with source volume (Figure 1b), or it may vary with the source volume (Figure 1c) where scale effects are significant. Aggregated observations of historical debris flows, compiled by Corominas (1996) and Rickenmann (2011), illustrate the general trend of decreasing travel angle (signifying increased mobility and a decrease in effective flow resistance) as source volume increases. While there is a lack of consensus in the literature, collisionality (e.g. Armanini 2013), fragmentation (e.g. Bowman et al. 2012; Caballero et al. 2014), pore pressure diffusion lengthscales (e.g. Iverson 2015; Kaitna et al. 2016), and thermal effects (e.g. Voight & Faust 1982; Goren & Aharonov 2007; Alonso et al. 2016; Fischer et al. 2018) amongst other hypotheses (e.g. effects at the laboratory scale such as side wall effects and air drag; Bryant et al. 2015; Kesseler et al. 2020) have been investigated as potential mechanisms through which larger volume landslides achieve higher mobility.

Experimental flume flows using dry granular material have shown that when the rheology of the flow is very simple, the runout behavior can be straightforwardly related to general physical parameters like slope angle, basal friction and grain size (e.g. Mangeney et al. 2010) or predicted using depth-averaged models (e.g. Bryant et al. 2015). Flows on fully saturated or initially saturated materials have shown rheological changes with source volume (e.g. de Haas et al. 2015), fines content or moisture content (e.g. Kaitna et al. 2014; Hürlimann et al. 2015; Zhou et al. 2018).

Numerical simulations of landslide runout offer the ability to release a source volume, propagate its flow over a 2D or 3D geometrical representation of the terrain, and provide estimates of inundation depth, velocity, and definition of the maximum distal reach of the debris for a given pairing of a resistance law and respective model parameter(s). In the case the moving mass is modelled based on an equivalent fluid concept (Hungr, 1995), the resistance law is chosen based on the nature of the flow. That can range from a granular flow to a fully liquefied flow for which the effect of pore fluid is of major importance.

For granular flows, the main source of flow resistance stems from particle friction and particle collisions. In dense granular flows, particle contacts are long-lasting and force chains develop. For natural flows in a frictional regime, the recently developed $\mu(I)$ rheology may be appropriate (Forterre & Pouliquen, 2008). A collisional regime can occur when the concentration of solids, represented by the volume fraction ν as the portion of total volume occupied by solid particles, is too low to maintain these long-lasting contacts (Bagnold, 1954; Jenkins & Savage, 1983). In a collisional regime the flow resistance comes not from friction but instead a collisional viscosity dependent on ν and the rate of collisions (e.g. Lun & Savage, 1986). The transition between the idealized regimes is not abrupt and the regimes are thought to exist simultaneously in the transition (Ancey & Evesque, 2000; Armanini, 2013). The interstitial fluid would also affect this collisional-frictional network of discrete particles.

With the addition of an interstitial fluid to a granular flow, particles are subject to both buoyancy and drag forces (Armanini, 2013; Iverson, 1997). Particle buoyancy reduces the interparticle stresses, which is represented on a macro scale by the concept of geotechnical effective stress $\sigma' = \sigma - u$, where σ is total stress, u is pore pressure. In a frictional continuum material, the shear resistance from friction is proportional to the effective stress (e.g. $\tau = \sigma' \tan\phi'$) - i.e. the Mohr-Coulomb criterion.

For a fully liquefied or low solids content flow, the effect of interstitial fluid may be more conveniently modelled by a non-Newtonian phenomenological flow law (Ancey, 2007), which is characterized by a distinct velocity profile. In both cases, pore pressure effects are typically considered to be constant during the duration of the flow. The validity of this assumption has been explored in Tayyebi et al. (2021), who suggest model choice should be guided through a consideration of two competing characteristic times: i) consolidation time and ii) propagation time. For scenarios in which the time of pore pressure dissipation is rapid in comparison to the travel time, the high permeability debris

is unlikely to retain excess positive pore pressure (e.g. Iverson 2015; Pudasaini et al. 2005; Pastor et al. 2014; Kaitna et al. 2016), permitting simpler models of pore pressure effects to be used. On the other hand, it may be appropriate for fully undrained models to simulate lower permeability flows, such as high water content slurries or liquefied debris. Debris flows with intermediate permeability between these two end members have the most computationally complex requirements for numerical simulation as the consolidation time and travel time can be of the same order.

Recent observations of large landslide events which include a transition from a granular flow to a liquefied flow (e.g. Walter et al., 2020; Shugar et al., 2021) and progress in monitoring of debris flows, including basal stresses (e.g. McArdell et al., 2007) and velocity profiles (Nagl et al., 2020) highlight the importance of the fluid in granular flows.

The addition of an interstitial fluid is therefore recognized to have a dominant impact on the mobility of the flow. Impulse releases of an opaque material from behind a rapidly opening gate have been performed by the USGS (e.g. Iverson et al. 2010) on a large scale with a laterally unconfined runout area or at laboratory scale (e.g. Hürlimann et al. 2015). Flows may also be triggered by moving water (e.g. Tsubaki et al. 1983; Hotta 2012; Lanzoni et al. 2017). A recirculating flume was used by Armanini et al. (2005) to host a long-duration debris flow from which grain-scale measurements of volume fraction and velocity could be taken.

However, experimental studies in which both the bulk-scale (runout) and grain-scale behaviour of identical granular material in a dry and saturated initial state are directly compared are rare. The comparison would provide a unique opportunity to test numerical simulation outcomes by first constraining the frictional properties of the material (i.e. matching the runout behaviour of the dry experiments of different source volumes) before independently evaluating the implementation of rheological models to account for buoyancy, fluid drag, and pore pressure affecting the frictional material. The relative contributions of each mechanism may be revealed by matching the volume scaling effects.

We performed a series of experiments on the end member cases of high permeability debris which is initially dry or initially saturated with the objective of defining the influence of interstitial fluid and landslide volume on the runout distance and the relative contributions of translation and spreading in a material in which excess pore pressure is not expected to occur. A monodisperse material was used to ensure no segregation of particle size would take place during flow which could alter the rheologic behaviour, other than that caused by variation in solid and fluid concentration. Granular material was selected of a large enough grain size to isolate the effects of buoyancy and drag on the flows and allow for particle-level observation of contact behaviour and flow regimes. Each flow was initiated from a well-defined state and observed comprehensively during the travel and arrest phases. Dry flows of the identical source volumes were also tested as a direct point of reference for comparison.

In the remainder of the manuscript, we first describe the research flume, instrumentation, and high-speed video analysis methods used for the experiments. The flow regimes of both dry and initially saturated 0.8 m^3 flows are then described and illustrated using representative frames and depth profiles. Next, velocity and volume fraction results are presented for volumes ranging between 0.2 to 1.0 m^3 to illustrate the variation in regimes. Finally, laser scanning results of the deposit morphology of each trial are used to explore the nature of the relationship between travel angle and source volume for both dry and wet flows.

2 Experimental Setup & Methodology

The experiments consisted of a series of granular flows in a large indoor testing facility (Figure 2). The 2.09 m wide flume features a 8.23 m long section inclined 30° from horizontal and a 33 m long horizontal runout section. For the entirety of the inclined por-

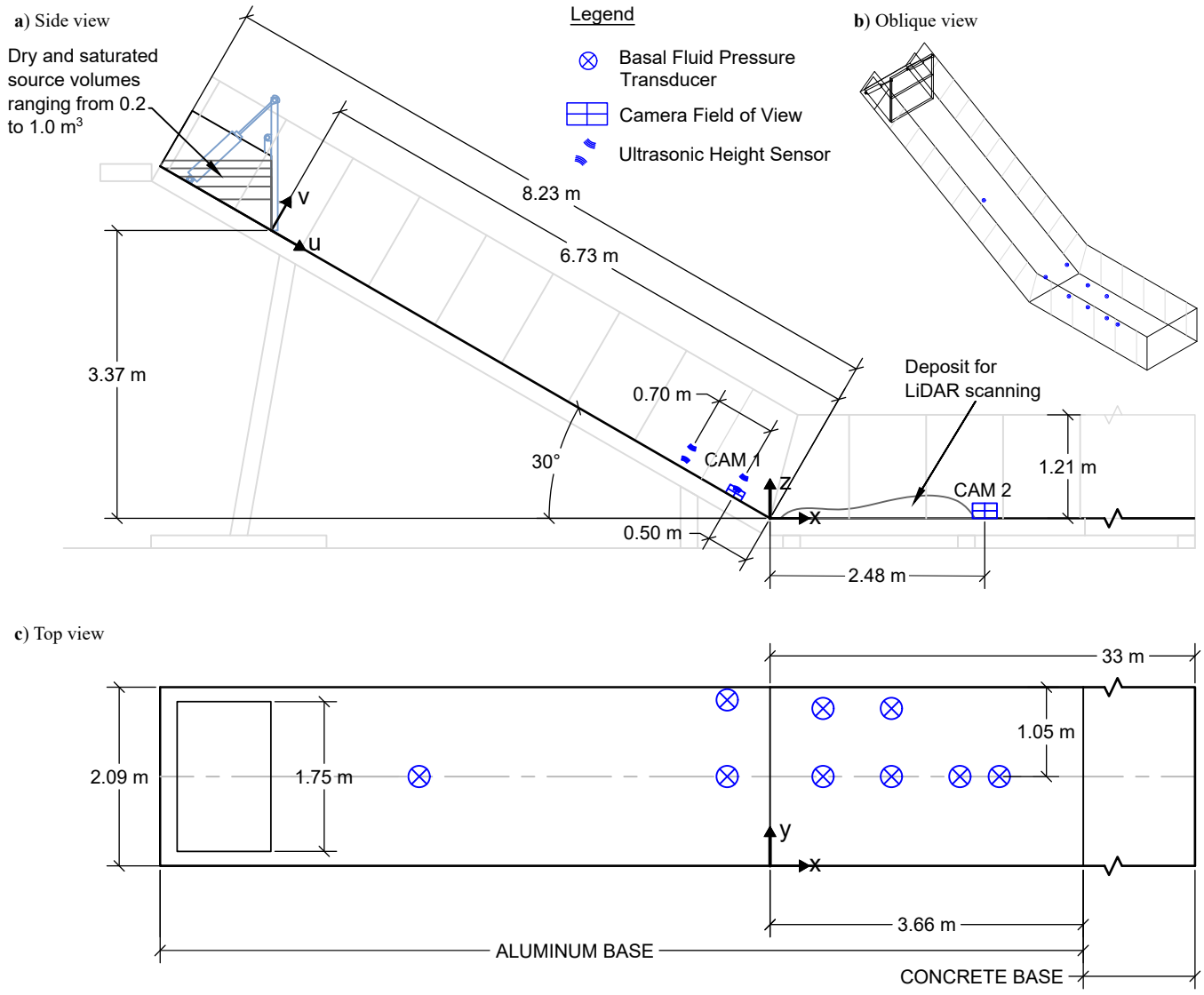

Figure 2. Diagram of (**a**) side profile, (**b**) oblique view, (**c**) top view of the experimental flume, illustrating the locations of high-speed video camera fields of view, basal fluid pressure transducers, and ultrasonic height sensors.

tion and for the first 3.68 m of the horizontal runout section, the base of the flume is constructed from bare aluminum and the side walls of the flume are glass to permit observation of the flows. Further down the flume, the base is constructed from smooth concrete. At the top, a release box with a hinged door can accommodate over 1.0 m^3 of saturated material. The door was rapidly opened using pneumatic cylinders to initiate the experiment, with the door moving clear of the material within 0.4 s. At the completion of the test, the final deposit shape was surveyed using a Faro Focus S 150 Light Detection and Ranging (LiDAR) scanner from two or more scanning positions.

2.1 Video Capture & Instrumentation

During the test, a Phantom v2512 high-speed video camera was located near the end of the inclined portion of the flume (indicated as 'CAM1' on Figure 2) to capture mature flow behaviour in the travel stage. The camera was oriented in a side-on configuration to observe through the transparent glass side walls, rotated such that the width of the image was parallel to the base of the flume. The camera was set to capture a 1280 x 800 pixel greyscale image at a frame rate of 7,500 - 10,000 fps (frames per second). A Tokina 100 mm f/2.8 Macro lens was used at its widest aperture to limit the depth of field and distinguish only the particles next to the glass side walls. The field of view was approximately 220 mm by 136 mm. A typical particle of 3.85 mm diameter was represented by a 23 pixel width in the resulting image.

As only one high-speed video camera was available, two initially saturated flows (0.4 and 0.8 m^3 source volumes) were repeated with the same camera and lens situated within the horizontal portion of the flume ('CAM2' on Figure 2). At this location, the camera was situated further back from the sidewall. The field of view was approximately 285 by 178 mm, with a typical particle represented by 17 pixels.

Nine fluid pressure transducer sensors were installed into the base of the flume to quantify the basal fluid pressure (Figure 2). The sensors (TE Connectivity model U5244-000002-14BG, 0 to 140 mbar range, manufacturer's stated accuracy 7 mm, total error band 18 mm) were threaded directly into the flume. The fluid could enter each sensor through seven holes of 2 mm diameter.

Two ultrasonic distance sensors (model S18UUAQ, Banner Engineering Corp., 2.5 ms response time) were mounted above the inclined section of the flume, along the flume centreline (Figure 2). These sensors recorded the flow height away from the influence of the glass sidewalls by measuring the distance between the sensor and the top of the flow, normal to the flume base.

The sensor signals were sampled and recorded at 2000 Hz. During the experiments, the pressure sensors were subject to noise considered to be resonance of the flume. The natural frequency of the flume structure was measured at approximately 140 Hz. To counteract this noise, the pressure sensor output signals were filtered using a 80 Hz low-pass Butterworth filter.

2.2 Materials and Preparation

Pseudo-spherical ceramic beads, manufactured by Saint-Gobain Norpro and marketed as Denstone 2000 Support Media, were used as the granular material for the experiments. These beads were chosen for their pseudospherical shape, relatively uniform diameter, and ability to be reused for multiple trials with minimal breakdown. The physical properties of a representative sample of 30 beads were measured and tabulated by Coombs et al. (2019). The beads were found to have an average diameter of 3.85 mm, grain sphericity of approximately 95%, and grain density of 2241 $\mathrm{kg\,m^{-3}}$. The bulk density was measured by Coombs (2018) as 1400 $\mathrm{kg\,m^{-3}}$, corresponding to a volume fraction of $\nu = 0.63$. According to the manufacturer, the hardness of the beads exceeds 6.5 on the Mohs scale. Triaxial tests conducted by Raymond (2002) gave effective friction angles of 33.7° at 20 kPa confining pressure.

The source volumes tested were comprised of 0.2, 0.4, 0.6, 0.8, and 1.0 m^3. In each of the dry and initially saturated states, the material was made level in the release box using a rake. In the initially saturated state, the pore spaces were inundated with water but ponding water on top of the beads was minimized.

3 High-speed video analysis and calculated quantities

High-speed video was used to observe the flow structure and to provide images for further analysis. In this section, we discuss the image analysis methods used to identify the velocity and volume fraction for each test.

3.1 Particle displacement and velocity

The Particle Tracking Velocimetry (PTV) method involves first identifying the particle locations in selected frames and then using a PTV algorithm to link individual particles in successive frames (Brevis et al., 2010; Gollin et al., 2017; Taylor-Noonan et al., 2021). In our experiments, the camera is oriented to match the inclination of the flume base to optimise the field of view, e.g. so the particle movement vectors (Figure 3a) are generally horizontal in the illustrations. The direction of gravity is noted on the figure.

The images were analyzed in sets of fifty (50) images. Each set was initiated at an interval of $t = 0.05$ s during the passage of the flow. Within each set, the frames were selected from the 7,500 - 10,000 fps video such that the analysed frames were $\Delta t = .0004$ s apart (equivalent to 2,500 fps). For a particle moving at 5 metres per second, the movement was 11.5 pixels and the resulting ratio of particle movement per frame to particle diameter was 0.52. For a particle moving at 1 metre per second, the corresponding movement was 2.3 pixels. The results were grouped into bins (shown by red lines on Figure 3) to prepare depth profiles of the quantities, each drawn parallel to the flume base with height equal to one average particle diameter. Each vector was decomposed into components parallel (streamwise) and perpendicular to the flume base.

Velocity profiles (Figure 3b) were calculated by averaging the components of each vector located within the bin, for all pairs of frames that comprise the set. From the profile of streamwise velocity u, the shear strain rate with respect to depth is defined here by $\dot{\gamma} \equiv \partial u/\partial z$. This quantity indicates relative displacement within the flow. The velocity of the lowest bin, adjacent to the flume base, was considered to be the basal slip velocity. As an example, Figure 4 presents the free surface and basal slip velocities for representative 0.8 m^3 dry and wet flows.

3.2 Volume Fraction

The volume fraction ν forms the basis for classification in Kinetic Theory and Extended Kinetic Theory (e.g. Lun, 1991; Jenkins, 2007; Chialvo et al., 2012). Randomly close packed spheres correspond to $\nu_{rcp} \approx 0.64$ (Allen & Thomas, 1999). Various contributors to EKT propose the frictional regime begins between $0.583 \leq \nu \leq 0.613$ when long-lasting particle contacts develop. Jenkins (2007) further divided the collisional regime at $\nu = 0.49$ into a 'dense collisional' and 'dilute collisional' regime based on a change in the likelihood of a particle collision. This proposed classification has been shown in the background of volume fraction plots in the following sections.

Here, ν was estimated using the method proposed by Capart et al. (2002), which considers the size and shape of Voronoï polygons drawn around the identified particle locations as the basis of estimation. The image plane is divided into regions, each containing one identified particle centroid location (Figure 3c). The regions are drawn such that all points in the region are closer to that identified particle than any other.

This method uses a roundness parameter $\xi = 4\pi A/P^2$ where A and P are the area and perimeter of the Voronoï polygon around the particle, respectively. The roundness parameter ξ is calculated for all the particles in a bin over all the frames in each set. Voronoï

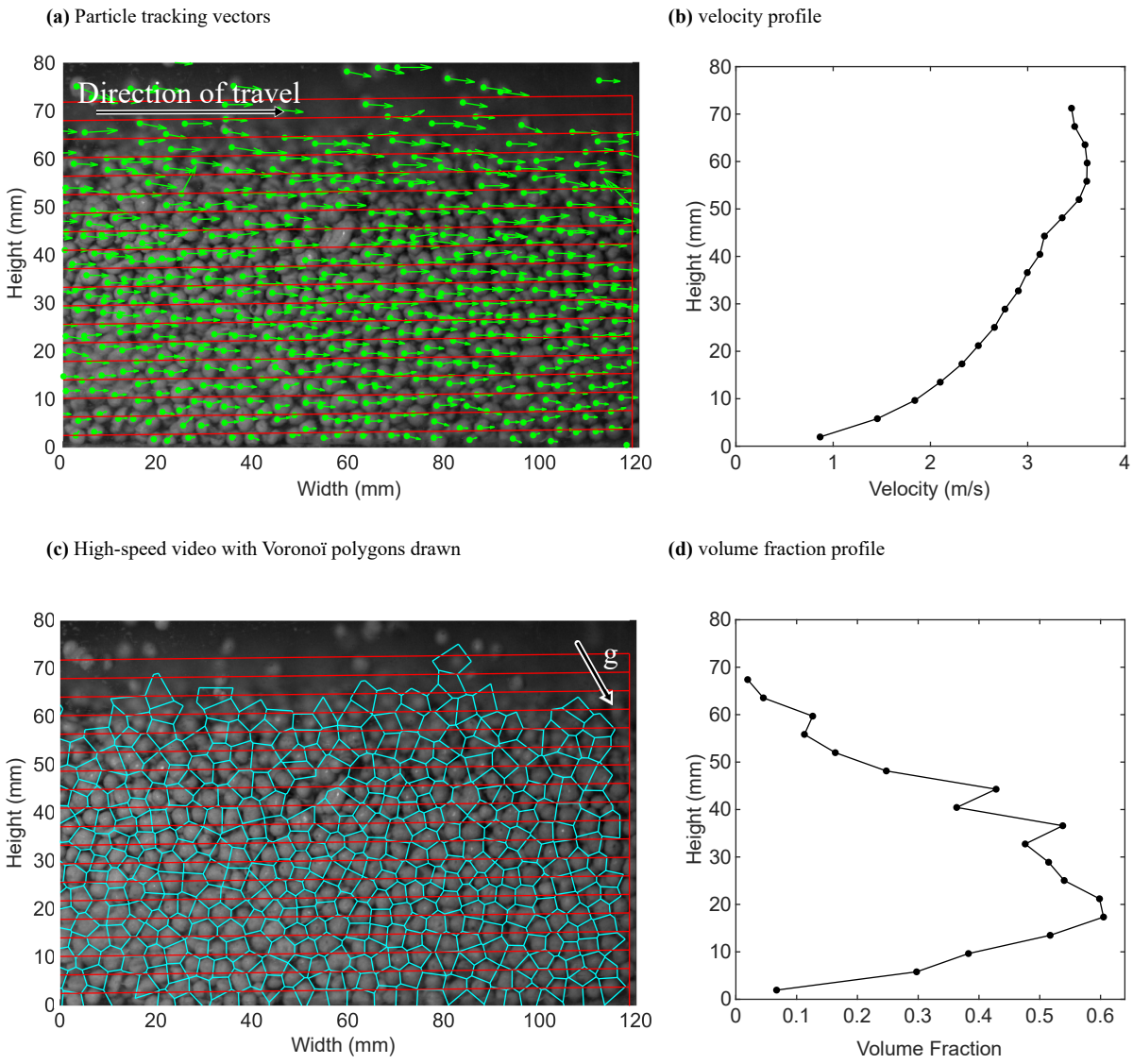

Figure 3. Representative video analysis and calculated profiles using PTV for 0.8 m^3 dry flow at peak flow height, illustrating (**a**) displacement vectors (green arrows) identified by PTV within bins drawn parallel to flume base (in red), (**b**) velocity profile calculated from displacement vectors within each bin, (**c**) Voronoï polygons drawn around particle locations for use in volume fraction estimation method, and (**d**) estimated volume fraction profile.

polygons which share an edge with the analysis area of interest were disregarded, as the shape of these polygons may have been 'clipped' by the analysis area of interest. Before inclusion into the average, each Voronoï polygon was assessed for size and shape; Voronoï polygons with areas exceeding 2.5 times the area of an average particle or with a roundness parameter ξ below 0.70 were then discarded. Any polygon bordering a polygon which was discarded due to size or shape was not included in the average.

The volume fraction profile (Figure 3d) is estimated by:

$$\frac{\nu}{\nu_{rcp}} = \left(\frac{\xi - \xi_0}{\xi_{rcp} - \xi_0} \right)^{\beta}$$

where indices "rcp" and "0" designate the state of random close packing and the dilute state, respectively. For random close packing of spheres, $\nu_{rcp} \approx 0.64$ (Allen & Thomas, 1999). Capart et al. (2002) performed a calibration study for volume fractions in the range $0.20 \leq \nu \leq 0.55$ and found calibration constants $\xi_{rcp} = 0.84$, $\xi_0 = 0.72$, and $\beta = 3.5$. Volume fractions $\nu \leq 0.20$ are approximated by the point density method, also by Capart et al. This method was developed for the case where particles are observed against a rigid transparent wall, but calibrated with the average volume fraction in the cell. Thus, the method is expected to estimate the volume fraction away from the influence of the rigid wall.

As the flow inevitably contained some saltating particles above the flow, a threshold is required to define what is considered to be the body of the flow. For the purposes of further analysis and discussion in this paper, the flow height of the trials was set by the threshold $\nu = 0.20$ over height and time (Figure 4). Some manual adjustments were made to exclude particles which were not immediately beside the sidewall glass. This was judged by the shallow depth of field of the camera lens and the incident light. The top of fluid was manually marked on images at 0.05 second intervals for the wet flows.

4 Flow characteristics

We begin the comparison of dry and saturated flows through visual observations of flow structure, velocity, volume fraction, and pore pressure measured at the observation point near the end of the inclined section of the flume (the 'CAM1' location). The times examined are shown on Figure 4. The 0.8 m^3 volume is chosen for this comparison of typical anatomy of the flows as this source volume exhibits the system of flow regimes discussed throughout this paper but is not at the extreme of source volumes tested. Later sections of the manuscript explore the variability observed in larger and smaller volumes and full analysis of the resulting deposit morphology.

4.1 Dry flow

The flow regimes within a 0.8 m^3 dry flow are revealed by the velocity and volume fraction profiles as it passes the 'CAM1' location (Figure 5) at selected times t since door opening. The initial front of the debris flow is heralded by saltating particles (Figure 5a) with $\nu \approx 0.2$ and (basal) slip velocity in excess of 2.5 ms^{-1}. A high level of collisional activity is seen when reviewing the video. As the core approaches (Figure 5b), the volume fraction increases to approximately $\nu = 0.32$. The bottom of the flow slows and $\dot{\gamma}$ quickly increases. The slip velocity at $t = 1.74$ s is 1.8 ms^{-1}, while the surface velocity is 4.0 ms^{-1} with a flow height of 36 mm.

The peak flow height comprises a dense ($\nu > 0.49$) core above a collisional base with a higher magnitude of $\dot{\gamma}$. The peak flow height of approximately 52 mm is visible at $t = 2.59$ s (Figure 5c). The surface velocity is approximately 3.4 ms^{-1}, slower than at $t = 1.74$ s even though the flow height is higher. The slip velocity has reduced further to approximately 0.9 $m\,s^{-1}$.

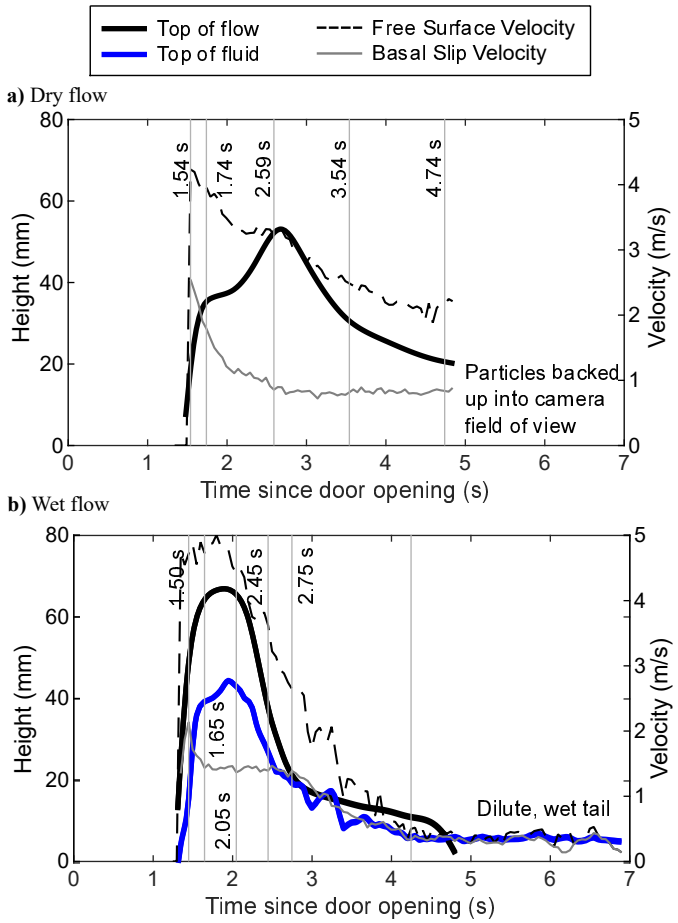

Figure 4. Flow heights (from side view camera) vs time, at 'CAM1' location near the end of the inclined section of flume, for representative 0.8 m^3 (**a**) dry and (**b**) wet flows. The initially saturated flow is taller, has the majority of the mass biased towards the front of the flow, and has a long thin tail portion. The top of fluid is below the top of flow at the time of peak flow height. The free surface and basal slip velocities are also shown.

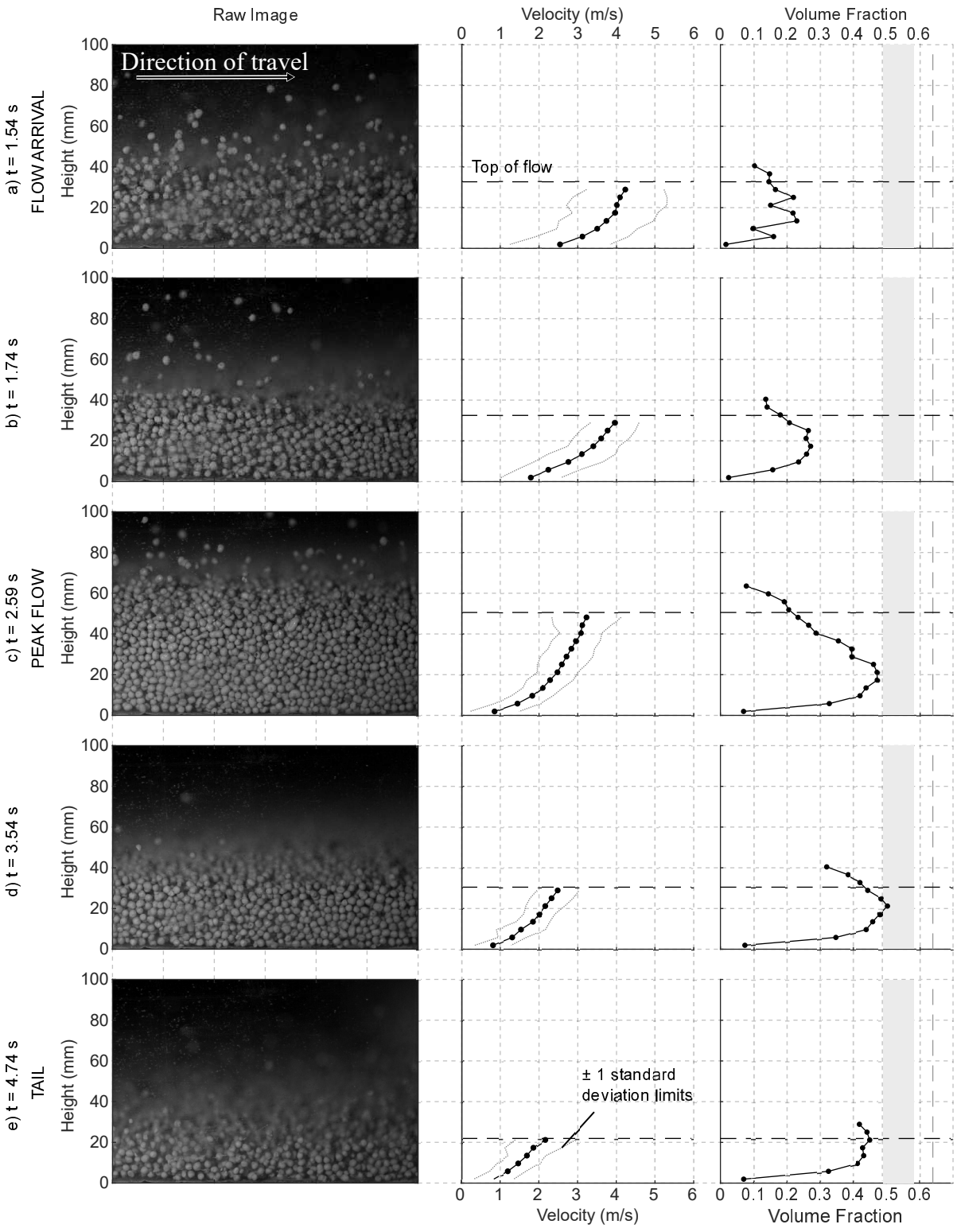

Figure 5. Anatomy of 0.8 m^3 dry flow at end of inclined section of flume ('CAM1'), showing a frame of video, the velocity profile with ± 1 standard deviation limits (in the 0.02 s observation time window), and the volume fraction ν at times (**a**) $t = 1.54$ s, (**b**) $t = 1.74$ s, (**c**) $t = 2.59$ s, (**d**) $t = 3.54$ s, (**e**) $t = 4.74$ s since door opening.

The volume fraction reduces gradually and the pressure at the base reduces after the body of the flow passes (Figure 5d). At $t = 3.54$ s, ν ranges up to a maximum of 0.51. At $t = 4.74$ s (Figure 5e), the flow height has reduced to approximately 21 mm and ν has reduced to approximately 0.28. The slip velocity remains at 0.8 ms^{-1} and the surface velocity has reduced to 2.2 ms^{-1}. At $t = 4.85$ s, the determination of the velocity for the 0.8 m^3 flow is not possible as particles at rest begin to back up into the camera's field of view. The runout morphology for this experiment is discussed in Section 6.

4.2 Saturated flow

The typical behaviour of a fluid saturated flow is presented in Figure 6 for the 0.8 m^3 volume. The front of the flow arrives before the fluid, similar to the unsaturated granular front observed in laboratory experiments by Leonardi et al. (2015) and Turnbull et al. (2015). In the early arrival stages of the core of the flow (Figure 6a), the top of fluid is seen at an approximate height of 30 mm while the flow height is approximately 43 mm. The free surface velocity exceeds 4.8 ms^{-1}, faster than the dry flow. The velocity profile shows a very high $\dot{\gamma} \approx 200\ \text{s}^{-1}$ near the flume base and minimal $\dot{\gamma}$ above the top of fluid. In rigid bed experiments, Armanini et al. (2005) also measured the highest $\dot{\gamma}$ near the base. Here, the flow is dilute, with identified volume fractions typically ranging between 0.3 and 0.4.

By $t = 2.05$ s, the flow height and the top of fluid are at their peak (Figure 6c), while the surface velocity has decreased to 4.5 ms^{-1}. The concentration of shear near the base of the flow continues. The density is less than the dry flow and is further reduced near the top of flow. Below the top of fluid, the maximum volume fraction, $\nu = 0.52$. In the portion of the flow above this, $\nu = 0.21$.

The top of fluid is coincident with the surface at $t = 2.75$ s (Figure 6e) as the tail of the flow passes 'CAM1'. The flow is relatively dilute with $\nu = 0.32$. The slip velocity reduces from 1.6 ms^{-1} at $t = 2.75$ s to 0.4 ms^{-1} at $t = 4.00$ s, at which time the flow is only two particles high. This is in stark contrast to the tail end of the dry flows, where the slip velocity is seen to be relatively constant (Figure 4).

Overall, the partitioning into a head section, frictional core, collisional base, and tail section is more pronounced for a wet flow then dry flow of the same volume.

A similar, repeat, test was carried out for the 0.8 m^3 initially saturated flow, with the high-speed video camera set at the 'CAM2' location (Figure 2) on the horizontal runout portion of the flume. The results show that the flow arrives in a dense ($\nu > 0.49$) state at the residual water content with a free surface speed of approximately 2.6 ms^{-1} (Figure 7a), which is approximately half that at the time of peak flow at the upstream 'CAM1' position. The peak flow height is over 100 mm, approximately two-thirds greater than at 'CAM1'. This shows that the material has laterally compressed following the change in slope. $\dot{\gamma}$ is highest near the base.

The top of fluid rises quickly to 102 mm above the flume base at $t = 2.40$ s (Figure 7b). A reduction in the volume fraction occurs simultaneously, especially near the top of the flow. As the core passes and the tail comes into view at $t = 3.00$ s (Figure 7c), the velocity decreases throughout the depth profile. The density increases in the lower portion of the flow. Later, the flow arrests completely while the tail is in the view of the camera.

4.3 Basal fluid pressures

During the initially saturated 0.8 m^3 flow, the centreline and side basal fluid pressure sensors at $x = -0.50$ m show similar peak pressure measurements. This leads to the conclusion that the flow is sufficiently mature at 'CAM1' to have recovered from the initial impulse of the granular collapse from the source box. Further down the flume at $x = +1.42$ m, the pressure traces are also generally similar from the centreline location to the side location.

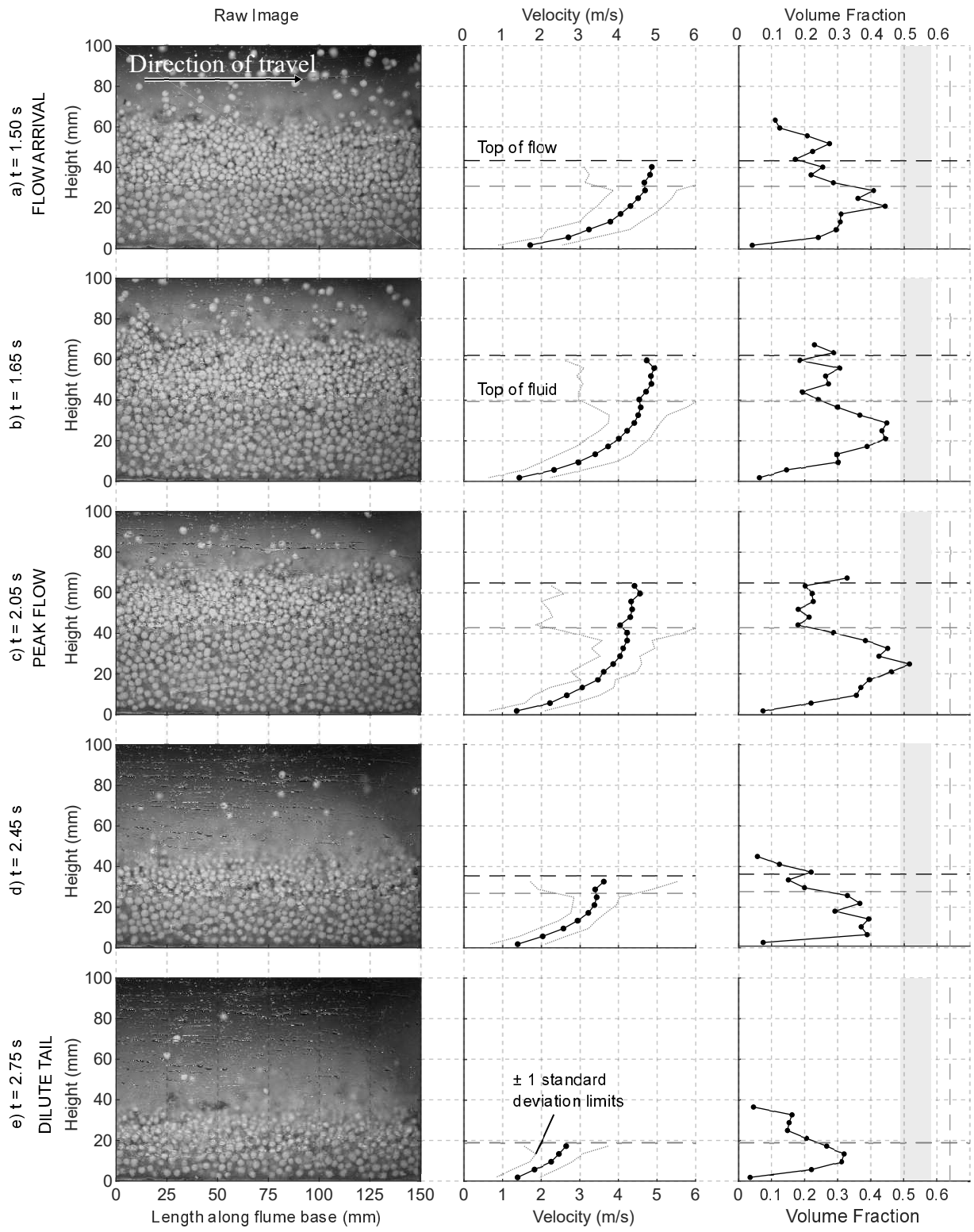

Figure 6. Anatomy of 0.8 m^3 initially saturated flow at end of inclined section of flume ('CAM1') showing a frame of video, the velocity profile with ± 1 standard deviation limits (in the 0.02 s observation time window), and the volume fraction ν at times (**a**) $t = 1.50$ s, (**b**) $t = 1.65$ s, (**c**) $t = 2.05$ s, (**d**) $t = 2.45$ s, (**e**) $t = 2.75$ s since door opening.

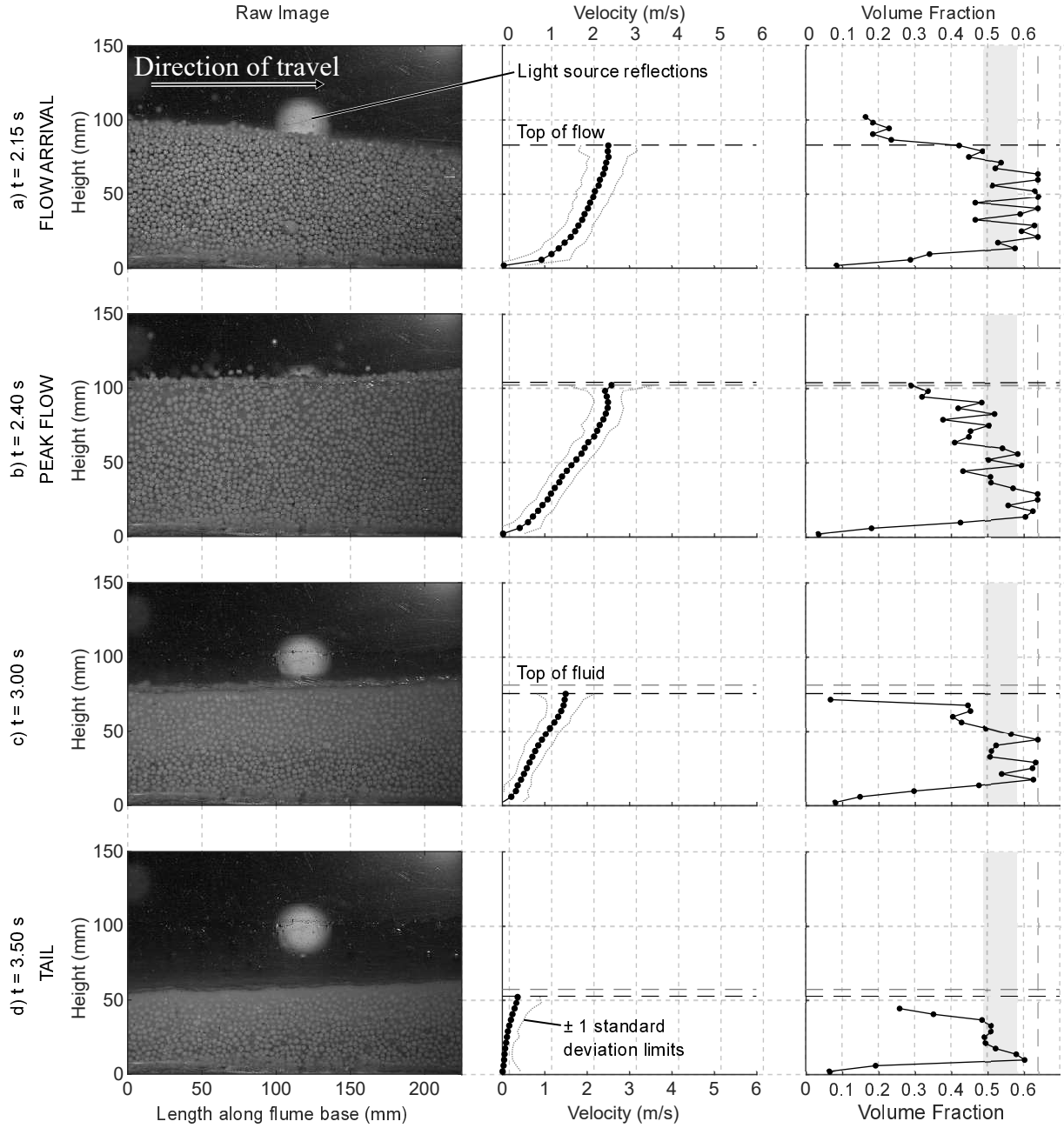

Figure 7. Anatomy of 0.8 m^3 wet flow in horizontal runout section of flume ('CAM2') showing a frame of video, the velocity profile with ± 1 standard deviation limits (in the 0.02 s observation time window), and the volume fraction ν at times (**a**) $t = 2.15$ s, (**b**) $t = 2.40$ s, (**c**) $t = 3.00$ s, (**d**) $t = 3.50$ s since door opening.

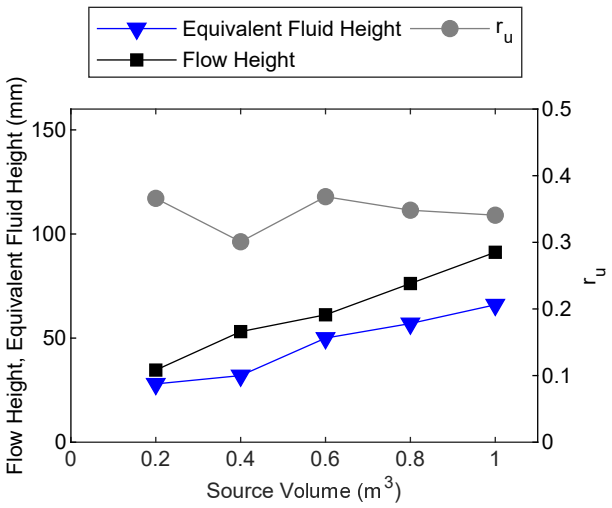

Figure 8. Peak flow heights and fluid pressures observed at $x = -0.50$ m along centreline for initially saturated trials, with equivalent fluid height remaining below flow height over range of source volumes tested. The pore pressure ratio r_u is defined here as the ratio of fluid pressure to the total vertical pressure.

The visually-identified top of fluid at the side of the flow can be compared to the measured basal fluid pressure P at the centre of the flow, expressed as an equivalent bed-normal fluid height $H = P/\rho_w g \cos\theta$, where the density of water $\rho_w = 1000$ kg $\cdot$ m^3, the slope angle $\theta = 30°$ and $g = 9.81$ m $\cdot$ s^{-2}. Here, the height H is similar between the visually-identified flow height (at the side wall) to the ultrasonic flow height sensor (at the centreline). The equivalent height of the basal fluid pressure is equal to the the height of the fluid, indicating that the matrix fluid pressures did not exceed the equivalent hydrostatic regime.

The basal fluid pressures consistently increase across the four sensors installed on the horizontal runout portion. The highest pressures observed are at the furthest distance from the release box. This is attributed to the increasing flow height as the front of the flow slows and the rear of the flow cascades over. Good agreement is seen between the equivalent fluid height from the sensor at $x = +2.68$ m and the top of fluid. The wet flow is subject to contraction during the arrest phase but the basal fluid pressures do not increase above hydrostatic.

5 Effect of varying source volume

In this section, we expand on the comparison of dry and initially saturated flows using observations of flow thickness, velocity, volume fraction, and pore pressure measured at the observation point near the end of the inclined section of the flume (the 'CAM1' location) for source volumes ranging between 0.2 to 1.0 m^3. This comparison is conducted to look at grain-scale mechanisms controlling the flow structure that may give rise to scale effects with flow volume.

5.1 Flow thicknesses and fluid pressures

As source volume increased through the tested range of 0.2 to 1.0 m^3, the observed maximum flow thickness at $x = -0.50$ m ('CAM1') increased from 38 to 51 mm for the dry flows and from 30 to 79 mm for the initially saturated flows.

As shown in Figure 8 at $x = -0.50$ m, the maximum equivalent bed-normal fluid height (as calculated in Section 4.3) is equal to the peak flow height for the range of initially saturated source volumes tested. This suggests the matrix fluid pressures did not exceed the equivalent hydrostatic regime. The pore pressure ratio r_u, defined here as the ratio of fluid pressure to the total vertical pressure, ranges between $[0.36 : 0.44]$.

5.2 Behaviour at peak flow height

In Figure 9, the time of peak flow height passing 'CAM1' is selected as a basis for comparison between the flows. This is the time when the flow is at its thickest and most dense state, and therefore the transport rate of mass is highest. A review of the profiles, discussed in detail below, provides information on the state of flow at the end of the incline as well as the partitioning of particles between highly shearing, lightly shearing, and collisional regimes.

At the time of peak flow height passing 'CAM1', the velocity profile of each of the initially saturated flows ("wet") is faster than that of the dry flows. The overall velocity of the wet flows increases as source volume increases, with the top of the core of the 1.0 m^3 flow attaining a speed exceeding 5.0 ms^{-1}. Wet flows of all volumes are each seen to have a very high $\dot{\gamma}$ near the base of the flow. The opposite is noted for the dry flows, which are seen to be slower for each height in the flow as source volume increases.

Two forms of velocity profile were fit to each flow as best possible. Firstly, in the form of Bagnold (1954):

$$u(y) = a\left[h^{3/2} - (h-y)^{3/2}\right] + b$$

where h is the flow height and a, b are best-fit constants. Secondly, a logarithmic velocity profile $u(y) = c \ln y + d$, where c, d are best-fit constants, representing a fully turbulent hydraulic flow. The velocity profiles of the dry flows are well represented by the Bagnold profiles, as expected for dense granular flows following the $\mu(I)$ rheology (Forterre & Pouliquen, 2008). For the wet flows, the fit quality of the Bagnold profile decreases as flow volume increases. The logarithmic profile has a higher quality of fit than the Bagnold profile above 0.4 m^3, and matches well through 0.4 to 0.8 m^3 range. The fit quality decreases for the 1.0 m^3 wet flow, suggesting a variation of flow regime with depth. The shape of the velocity profiles, with nonzero basal slip velocity and a decreasing $\dot{\gamma}$ with increasing height above the base, is similar to the solid bed flows of Armanini et al. (2005) (Figure S1, supporting information). Velocity profiles of natural debris flows on a non-erodible bed measured by Nagl et al. (2020) indicate a nonzero basal slip velocity and a mostly concave-up velocity profile during a flow event, with complex deposition and re-mobilization of material during a sequence of surges.

At 'CAM2' after the change in slope, the 0.8 m^3 wet flow maintains this highly shearing flow which transports material (at residual water content) to the front of the flow. By comparison, the 0.4 m^3 wet flow displays minimal shearing at the same location.

Across the range of source volumes, the volume fraction profiles at the time of peak height passing 'CAM1' (Figure 9) for the dry flows display a similar shape as the 0.8 m^3 flow discussed above. The maximum volume fraction of the core increases with source volume. Each volume of wet flows displays a similar shape as the 0.8 m^3 flow, with a reduction in volume fraction above the top of fluid. The 0.2 through 0.6 m^3 dry flows each are entirely in a collisional regime when assessed by volume fraction. The 0.8 and 1.0 m^3 dry flows each have portions exceeding $\nu = 0.583$, indicating a frictional regime. While the maximum volume fractions of the wet flows increase slightly with source volume, the wet flows each have a lower maximum volume fraction than the dry flows of the same source volume and all remain in a collisional regime. For the dry flows, the volume fraction near the base is relatively consistent over the range of 0.2 to 0.8 m^3. For the 1.0 m^3

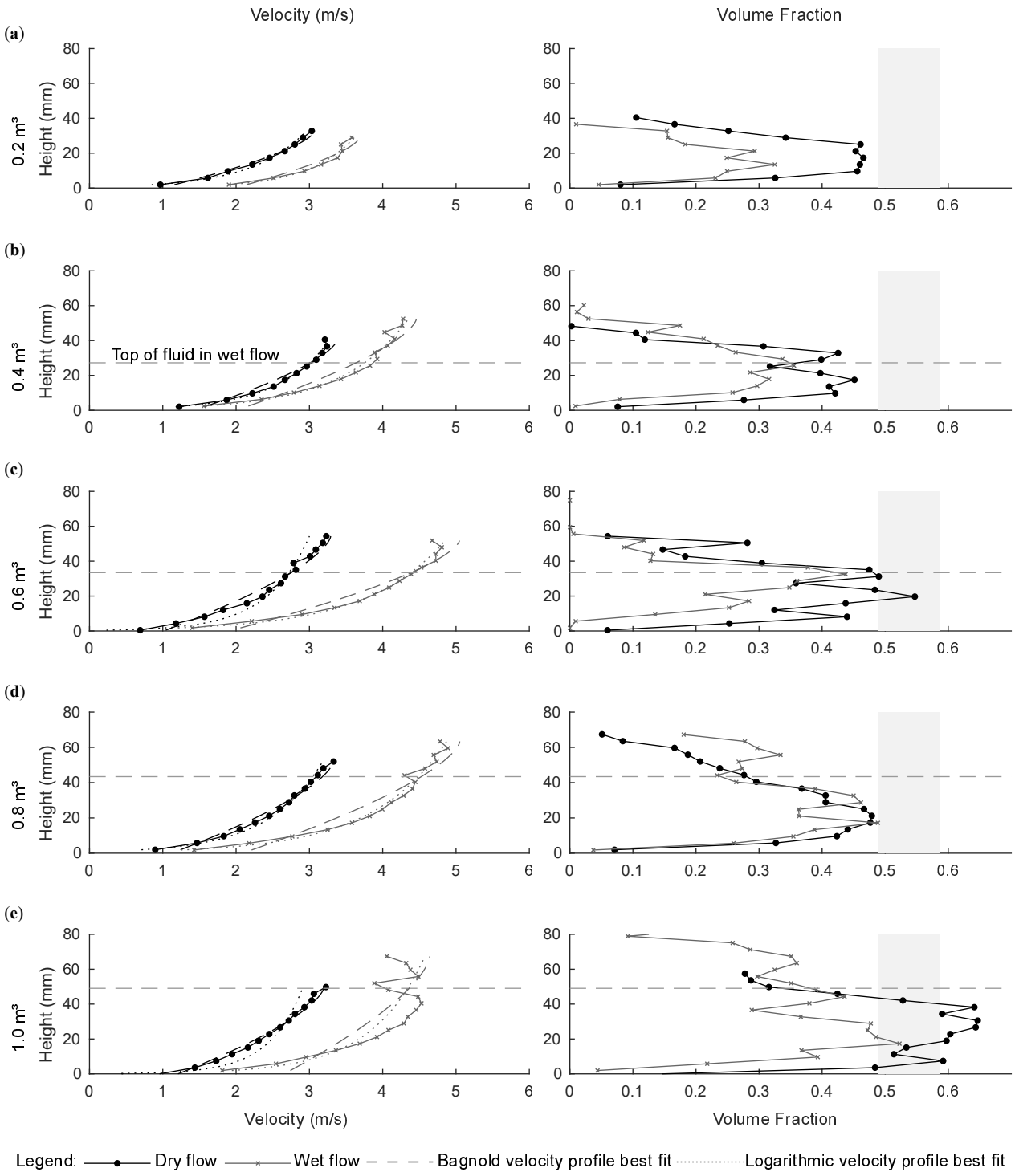

Figure 9. Comparison of depth profiles of streamwise velocity and volume fraction at the time of maximum flow height for (**a**) 0.2 m^3 to (**e**) 1.0 m^3 flows in 0.2 m^3 increments. Best-fits of Bagnoldian and logarithmic velocity profiles are shown in dashed and dotted lines, respectively. The shading in the volume fraction plot represents the dense collisional regime ($0.49 \leq \nu \leq 0.583$).

flow, the dense region is seen to extend down to near the flume base, suggesting that the increased confining pressure of the thicker frictional core has suppressed the collisional base. The wet flows displayed a reduction in volume fraction near the base over the range of source volumes, coincident with a high $\dot{\gamma}$.

The basal and free surface velocities and depth-averaged volume fractions are detailed for each trial in Table S1, in the supporting information. Using these parameters, all flows were classified as collisional flows by the Inertial Number I (e.g. Turnbull et al., 2015; Forterre & Pouliquen, 2008). The strong variation of $\dot{\gamma}$ with depth seen in the wet flows suggests that the Inertial Number varies with depth in the flows, and classification from a depth-averaged Inertial Number does not reliably describe the grain-scale behaviour seen in the wet flows.

5.3 Longitudinal distribution of regimes

We note that the core region of the initially saturated flows appears to enter an efficient mode of transport that increases in velocity with flow thickness, to a greater extent than would be expected according to Bagnoldian theory. Hence, the size of this core region relative to the total flow size is examined here. The partitioning into regimes along the length of the flow from head to tail can be assessed through plots of the measured quantities for each analysis interval and depth bin. Figure 10 shows the volume fraction results and Figure 11 shows the velocity results in a contour plot format where the contour lines represent isovelocity lines. $\dot{\gamma}$ can be inferred from the vertical distance between the isovelocity contour lines: isovelocity lines closer together represent a higher shear rate. Where the lines are parallel to the x-axis, that portion of the velocity profile is constant with time.

The volume fraction of the dry flows (Figure 10) shows partitioning of the flow into a dilute, saltating head preceding the front, a dense core where volume fraction increases with source volume, and a gradual of reduction of volume fraction towards the tail. During this transition period, the velocity results show only gradual changes with time (Figure 11). Geometric similarity of the flow height over time is evident across the range of source volumes and the change in flow height between core and tail is gradual. In contrast, for the wet flows the regime of the tail is distinct from the core for both volume fraction and velocity (Figure 10 and Figure 11, respectively).

The initially saturated flows each display a period with near-constant velocity in the base of the flow (Figure 11), with the duration of this increasing with source volume. Only a short period of near-constant velocity in the base is observed within the 0.2 m^3 flow, increasing to 0.9 s for the 1.0 m^3 flow. The maximum $\dot{\gamma}$ near the base does not vary significantly with source volume, suggesting that the wet flows find a preferred, efficient state of flow. The velocity profiles remain near-constant as the flow height reduces until seemingly falling below a critical threshold where the velocity abruptly reduces and the tail begins. This phenomenon is also visible on a plot of the slip velocity over time from the flow front (Figure 12) as a distinct plateau for the wet flows but not for the dry flows.

The decrease in velocity from core to tail was greater for the wet flows than the dry flows. An effect for the deceleration of the wet flows is thought to be due to surface tension between the liquid phase with the flume base and sidewalls. At this stage, the tail portions of the initially saturated flows are slow moving and of low volume fraction and minimal thickness. Some ceramic beads remained on the flume surface at the end of the experiments until the remnant water evaporated. The material partitioned to this slow-moving tail would reduce the volume available to be transported at high speed in the core section of the flow. This is in accordance with the description of 'starving' avalanches by Bartelt et al. (2007).

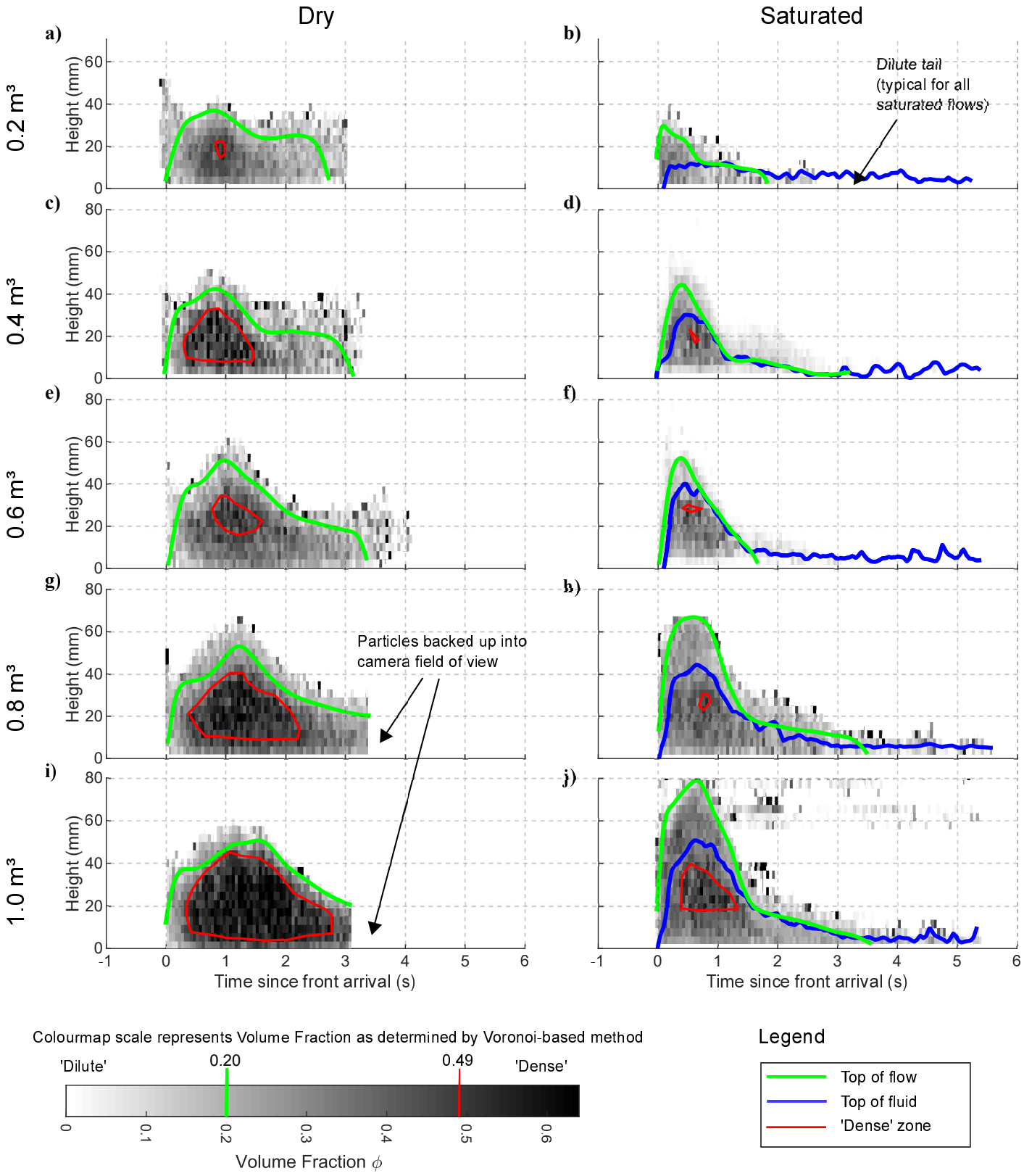

Figure 10. Height (y)-Time (x)-Volume Fraction (color scale) plots for dry and saturated trials over the range of source volumes, illustrating the formation of a dense granular core for dry flows and a comparatively dilute core for wet flows. Both flows exhibit a reduction in volume fraction near the rigid flume base.

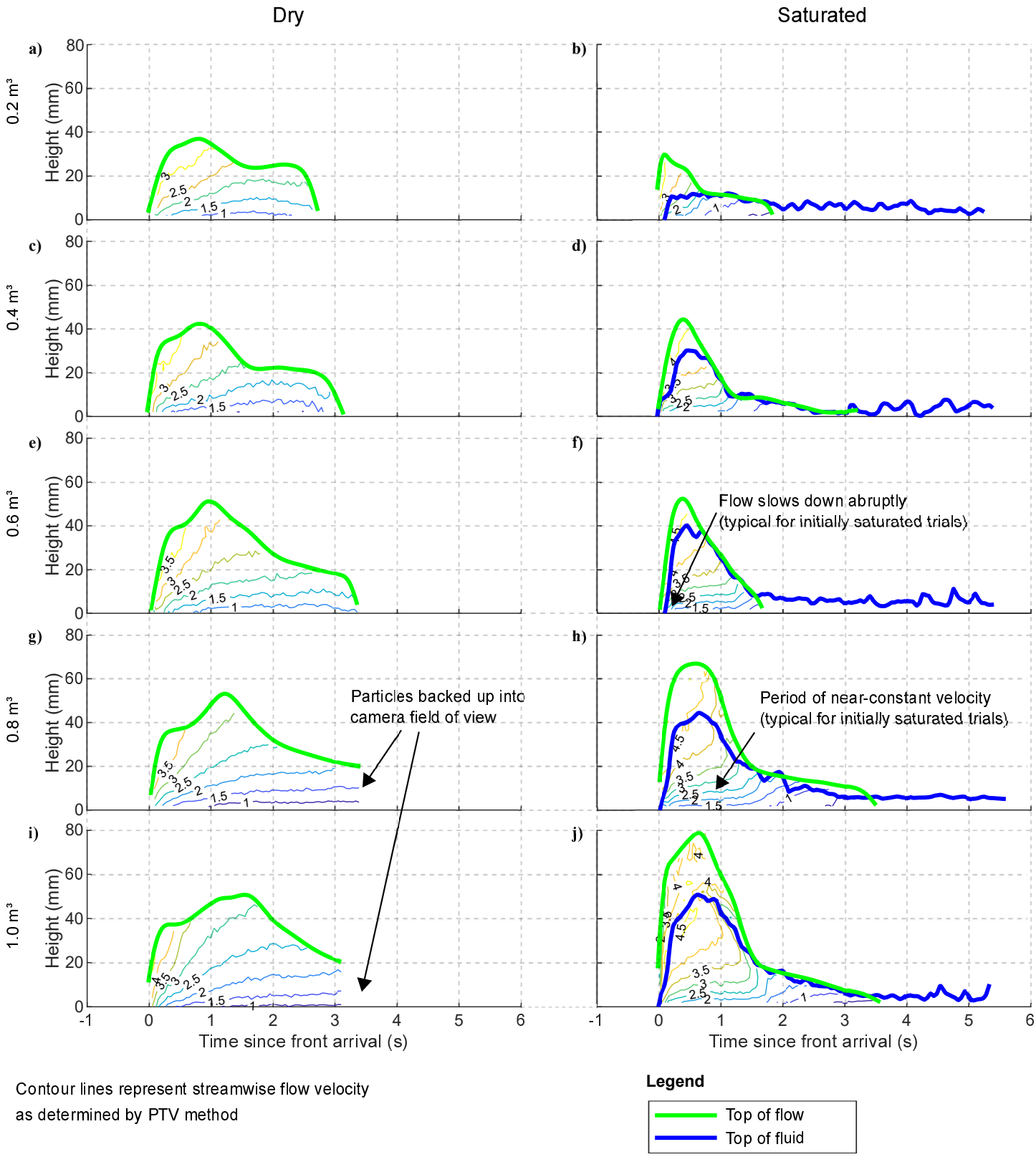

Figure 11. Height (y)-Time (x)-Velocity (color scale) plots for dry and initially saturated trials over the range of source volumes, illustrating a period of near-constant velocity near the base of the flume for the initially saturated state, suggesting that the flows find a preferred, efficient state of flow for translation and until the core height reduces below a critical threshold.

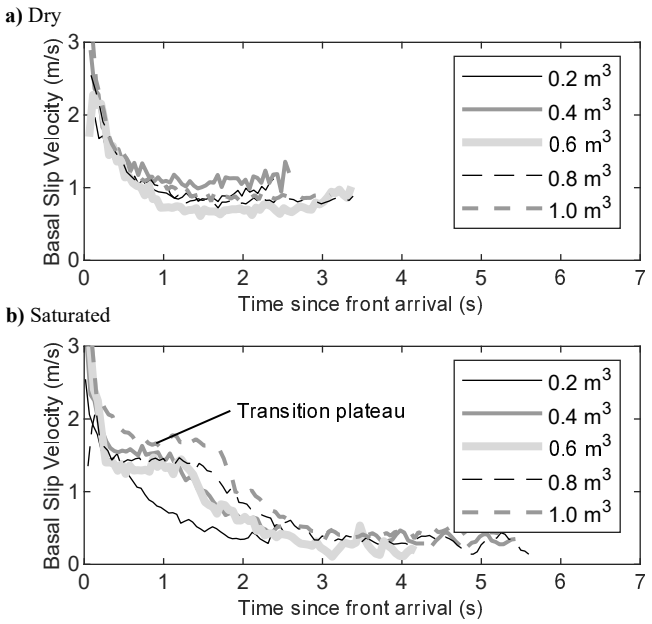

Figure 12. Comparison of basal slip velocities at end of incline for (**a**) dry trials illustrating the gradual decline in basal slip velocity and (**b**) initially saturated trials, illustrating a 'step' phenomenon where the velocity remains constant while the core passes, then quickly reduces to a slow speed (<0.5 ms^{-1}) for the tail.

6 Variation of morphology of resultant deposit with source volume

In the previous section, observations at the grain-scale revealed localized shearing at the base and evolution of volume fraction zones with flow height. In this section, we explore the changes in bulk behaviour, as reflected in the deposit morphology, for the varied source volumes.

The deposit morphology for each of the five dry and five saturated flow volumes, captured using LIDAR scanning, is presented in Figure 13. The profile of deposit morphology illustrates geometrical similarity (centre-of-mass travel distance, shape and slope angle of the deposit) over the range of source volumes for dry flows. In contrast, the initially saturated flows display markedly increased runout distances as source volume increases. Runout statistics, illustrated schematically in Figure 1a, can be used to summarize the resultant deposit morphologies (Figure 14). The frontal extents of the flow are considered in Heim's Ratio H/L (Figure 14a). Heim's Ratio remains relatively constant for dry flows but decreases significantly for initially saturated flows, indicating increased mobility with volume. Parez & Aharonov (2015) decompose the runout into translation of the centre-of-mass, related to an apparent friction coefficient, and forward spread S_f ahead of the centre-of-mass (Figure 14b). A slight increase in the forward spreading distance is seen for dry flows, commensurate with geometric similitude. For the initially saturated flows, a much larger increase of the forward spreading distance with volume occurs, the majority of which is from translation of the centre-of-mass.

The travel angle statistics summarize the translation of the centre-of-mass (Figure 14c), with a lower travel angle indicating a general increase in mobility. For the dry tests, a relatively consistent travel angle of 27.1° to 28.1° was calcuated over the range of source volumes tested. For the wet tests, the travel angle reduced significantly from 25.7° for a source volume of 0.2 m^3 to 20.1° for a source volume of 1.0 m^3. This marked decrease

(a) Dry trials

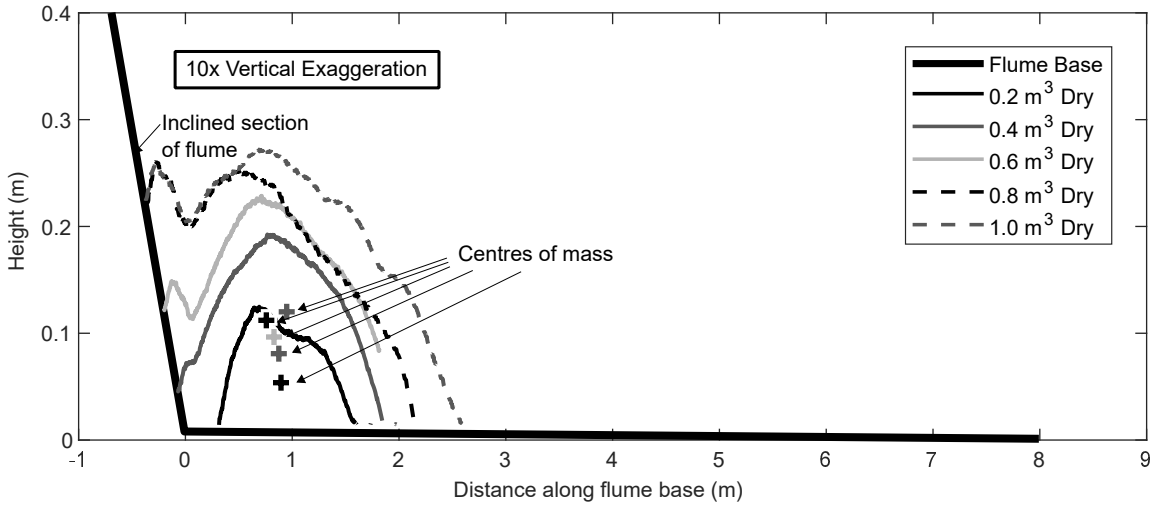

(b) Initially saturated trials

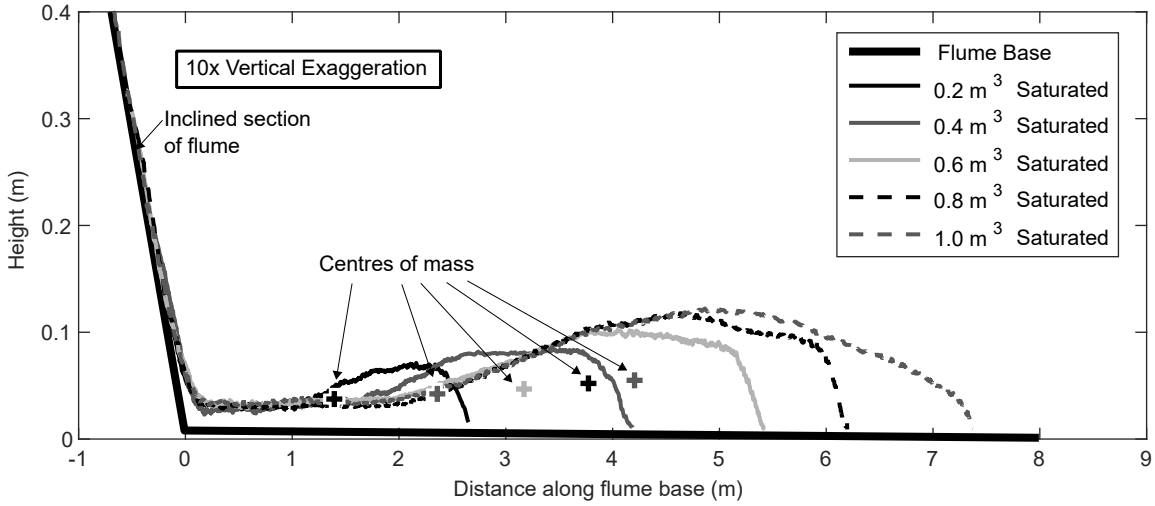

Figure 13. Comparison of resultant deposit morphology profiles for (**a**) dry and (**b**) initially saturated trials, with calculated centres of mass indicated.

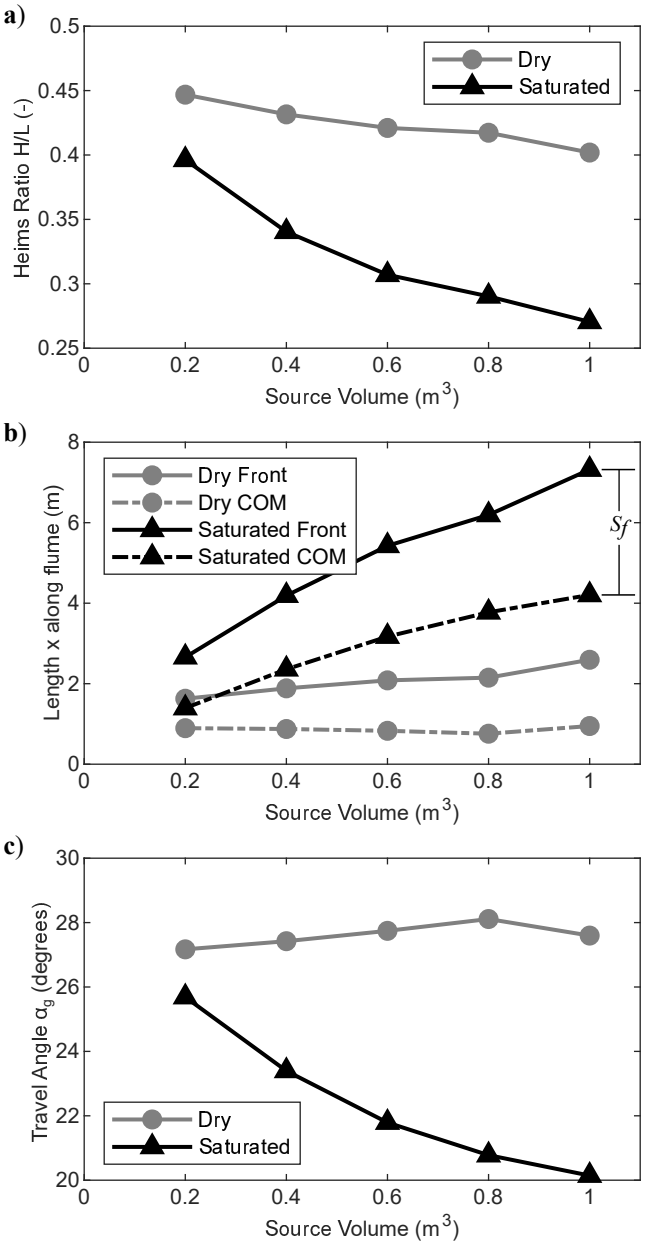

Figure 14. Comparison of summary statistics of mobility, showing (**a**) Heim's ratio from top of source volume to distal reach of deposit, (**b**) position of front extent of deposit and centre-of-mass of deposit, illustrating the relative contributions of each to total runout, and (**c**) travel angle between centres of mass.

indicates that one or more physical processes within the rheology of the wet flows are affected by experiment size.

7 Conclusions

A series of monodisperse granular flows was released within a large laboratory flume to define the effect of landslide volume on the runout distance and the relative contributions of translation and spreading in the end member case of high permeability debris. Both dry and initially saturated states were tested and the source volume was systematically varied from 0.2 to 1.0 m^3 in 0.2 m^3 increments. The use of high permeability debris retained the possible influences of particle buoyancy and fluid drag but was confirmed to not result in basal fluid pressures that exceed hydrostatic conditions. The tests exhibited marked differences in runout distance and flow regimes as observed by high-speed video between dry and initially water saturated conditions. The initially saturated flows displayed an increase in flow velocity and runout distance as flow source volume increased. This increase in total mobility was seen to come more from translation of the centre-of-mass than spreading at the front.

For particles considered as a frictional continuum, the effect of interstitial fluid is through reduction in the contact stresses between particles. In this case where the interstitial fluid pressures did not exceed hydrostatic conditions, the effect would be limited to particle buoyancy and not subject to scaling with flow thickness. Fluid drag can also occur if the interstitial fluid is travelling at a different speed than the particles.

The results show that the lower portions of the wet flows have decreased in volume fraction significantly and have entered a collisional regime. $\dot{\gamma}$ is highest in the collisional zone near the base. The variation in flow speed and translation distance may be caused by partitioning of the source volume into generally 1) a highly shearing base, 2) a core section above and 3) a slow tail section. Energy is only expended by the flow when $\dot{\gamma}$ is nonzero. Energy expenditure is concentrated in the base of the flow and the tail section starves the flow of fluid and particles as the flume surface is wet and the particles remain by capillary forces. The remainder of the source volume is transported in the core very quickly with little energy expenditure, and is the prime contributor to the long runout distances observed. This system of flow regimes is considered to be a preferred, efficient state of flow.

The scaling effects are postulated to arise when varying source volumes are not split into these regimes proportionally. The experiments showed the highly shearing base to be of similar height across the series of wet flows and the tail sections appeared similar as well.

The data show that the flow resistance of fluid-saturated flows may be defined by particle collisions and interactions with interstitial fluid on a local scale and preclude depth-averaged or continuum approaches. Physical experiments linking particulate behaviour to bulk response are required to fully validate and calibrate conceptual and numerical models of collisional and multiphase behaviour.

The results suggest some potential applications to granular mass flows in the field, e.g. debris flows. The shape of the velocity profiles (Figure 9) for the identical sediment mixture are useful to constrain an appropriate rheology to describe several aspects of the flow behavior of both dry and wet granular flows. The shape of the velocity profile is especially useful for choosing an appropriate rheology (or friction relation) used in depth-averaged runout models of debris flows. Such models (e.g. Barnhart et al. 2021) are used for hazard mapping, interpretation of recent events and also for impact calculations for designing mitigation measures. The shape of the velocity profile is necessary to increase the accuracy of the depth-averaged momentum predicted by such models. Experiments to evaluate the influence of basal roughness on the velocity profile, which is beyond the scope of this study, would provide an additional data set to better understand the role of basal friction and basal slip on the shape of the velocity profiles. The observation that

the velocity profile changes with water content is also of interest for accurately determining the volume of a debris flow from depth recordings in cases where independent observations of the volume are unavailable. Solutions to this problem are rare, and until now the rheology (or more simply the friction relation) of a debris flow is assumed to be constant over the duration of an event (e.g. Schlunegger et al. 2009), or the variation of velocity with depth and time within a flow is not considered, resulting in systematic errors in estimating the instantaneous discharge and volume of a debris flow.

Flume experiments will remain useful for debris flow research for the foreseeable future. This data provides additional support to the conclusion that flow thickness matters, particularly for fluid saturated flows. This study begins to address the paucity of such experiments through the publication of a unique dataset that combines the detailed grain-scale visual observations of flow structure, velocity, and volume fraction, with the observed consequences in terms of effective friction and debris spreading. This unique dataset is publicly available on the Scholarsportal Dataverse repository to serve as a well-defined test scenario to assess the role of interstitial fluid in numerical runout models of debris flows.

Open Research

The data used in this research are archived in the Queen's University Dataverse (https://doi.org/10.5683/SP3/1ZCUI

Acknowledgments

This project is the result of a Leverhulme Trust International Network Grant (#IN-2016-041) "The Rosetta Stone Network: Physical testing towards a common understanding of debris flows". Funding for the first author provided by a NSERC Discovery Grant to the last author. The first author would like to thank Natalie Arpin, Branna MacDougall, Erica Treflik-Body, Megan McKellar, Andrea Walsh, Artur Sass Braga, Joshua Coghlan, Graeme Boyd, Hal Stephens and Richard Foley for their ideas and assistance in the laboratory.

References

Allen, S. M., & Thomas, E. L. (1999). *The structure of materials* (Vol. 44). Wiley New York.

Alonso, E. E., Zervos, A., & Pinyol, N. M. (2016). Thermo-poro-mechanical analysis of landslides: from creeping behaviour to catastrophic failure. *Géotechnique*, *66*(3), 202–219. doi: 10.1680/jgeot.15.lm.006

Ancey, C. (2007). Plasticity and geophysical flows: A review. *Journal of Non-Newtonian Fluid Mechanics*, *142*(1-3), 4–35. doi: 10.1016/j.jnnfm.2006.05.005

Ancey, C., & Evesque, P. (2000). Frictional-collisional regime for granular suspension flows down an inclined channel. *Physical Review E*, *62*(6), 8349–8360. doi: 10.1103/physreve.62.8349

Armanini, A. (2013). Granular flows driven by gravity. *Journal of Hydraulic Research*, *51*(2), 111–120. doi: 10.1080/00221686.2013.788080

Armanini, A., Capart, H., Fraccarollo, L., & Larcher, M. (2005). Rheological stratification in experimental free-surface flows of granular–liquid mixtures. *Journal of Fluid Mechanics*, *532*, 269–319. doi: 10.1017/s0022112005004283

Bagnold, R. (1954). Experiments on a gravity-free dispersion of large solid spheres in a newtonian fluid under shear. *Proceedings of the Royal Society of London. Series A. Mathematical and Physical Sciences*, *225*(1160), 49–63. doi: 10.1098/rspa.1954.0186

Barnhart, K. R., Jones, R. P., George, D. L., McArdell, B. W., Rengers, F. K., Staley, D. M., & Kean, J. W. (2021). Multi-model comparison of computed debris flow runout for the 9 january 2018 montecito, california post-wildfire event. *Journal of Geophysical Research: Earth Surface*, *126*(12). doi: 10.1029/2021jf006245

Bartelt, P., Buser, O., & Platzer, K. (2007). Starving avalanches: Frictional mechanisms at the tails of finite-sized mass movements. *Geophysical Research Letters*, *34*(20). doi: 10.1029/2007gl031352

Bowman, E., Take, W., Rait, K., & Hann, C. (2012). Physical models of rock avalanche spreading behaviour with dynamic fragmentation. *Canadian Geotechnical Journal*, *49*(4), 460–476. doi: 10.1139/t2012-007

Brevis, W., Niño, Y., & Jirka, G. H. (2010). Integrating cross-correlation and relaxation algorithms for particle tracking velocimetry. *Experiments in Fluids*, *50*(1), 135–147. doi: 10.1007/s00348-010-0907-z

Bryant, S. K., Take, W. A., & Bowman, E. T. (2015). Observations of grain-scale interactions and simulation of dry granular flows in a large-scale flume. *Canadian Geotechnical Journal*, *52*(5), 638–655. doi: 10.1139/cgj-2013-0425

Caballero, L., Sarocchi, D., Soto, E., & Borselli, L. (2014). Rheological changes induced by clast fragmentation in debris flows. *Journal of Geophysical Research: Earth Surface*, *119*(9), 1800–1817. doi: 10.1002/2013jf002942

Capart, H., Young, D. L., & Zech, Y. (2002). Voronoï imaging methods for the measurement of granular flows. *Experiments in Fluids*, *32*(1), 121–135. doi: 10.1007/s003480200013

Chialvo, S., Sun, J., & Sundaresan, S. (2012). Bridging the rheology of granular flows in three regimes. *Physical Review E*, *85*(2). doi: 10.1103/physreve.85.021305

Coombs, S. (2018). *A physical investigation of the flow structure and mobility behaviour of collisional granular landslides* (mathesis). Queen's University.

Coombs, S., Apostolov, A., Take, W. A., & Benoît, J. (2019). Mobility of dry granular flows of varying collisional activity quantified by smart rock sensors. *Canadian Geotechnical Journal*. doi: 10.1139/cgj-2018-0278

Corominas, J. (1996). The angle of reach as a mobility index for small and large landslides. *Canadian Geotechnical Journal*, *33*(2), 260–271. doi: 10.1139/t96-005

Dade, W. B., & Huppert, H. E. (1998). Long-runout rockfalls. *Geology*, *26*(9), 803. doi: 10.1130/0091-7613(1998)026<0803:lrr>2.3.co;2

de Haas, T., Braat, L., Leuven, J. R. F. W., Lokhorst, I. R., & Kleinhans, M. G. (2015). Effects of debris flow composition on runout, depositional mechanisms, and deposit morphology in laboratory experiments. *Journal of Geophysical Research: Earth Surface*, *120*(9), 1949–1972. doi: 10.1002/2015jf003525

Fischer, J.-T., Kaitna, R., Heil, K., & Reiweger, I. (2018). The heat of the flow: Thermal equilibrium in gravitational mass flows. *Geophysical Research Letters*, *45*(20). doi: 10.1029/2018gl079585

Forterre, Y., & Pouliquen, O. (2008). Flows of dense granular media. *Annual Review of Fluid Mechanics*, *40*(1), 1–24. doi: 10.1146/annurev.fluid.40.111406.102142

Gollin, D., Brevis, W., Bowman, E. T., & Shepley, P. (2017). Performance of PIV and PTV for granular flow measurements. *Granular Matter*, *19*(3). doi: 10.1007/s10035-017-0730-9

Goren, L., & Aharonov, E. (2007). Long runout landslides: The role of frictional heating and hydraulic diffusivity. *Geophysical Research Letters*, *34*(7). doi: 10.1029/2006gl028895

Hotta, N. (2012). Basal interstitial water pressure in laboratory debris flows over a rigid bed in an open channel. *Natural Hazards and Earth System Sciences*, *12*(8), 2499–2505. doi: 10.5194/nhess-12-2499-2012

Hungr, O. (1995). A model for the runout analysis of rapid flow slides, debris flows, and avalanches. *Canadian Geotechnical Journal*, *32*(4), 610–623. doi: 10.1139/t95-063

Hürlimann, M., McArdell, B. W., & Rickli, C. (2015). Field and laboratory analysis of the runout characteristics of hillslope debris flows in switzerland. *Geomorphology*, *232*, 20–32. doi: 10.1016/j.geomorph.2014.11.030

Iverson, R. M. (1997). The physics of debris flows. *Reviews of Geophysics*, *35*(3), 245–296. doi: 10.1029/97rg00426

Iverson, R. M. (2015). Scaling and design of landslide and debris-flow experiments. *Geomorphology*, *244*, 9–20. doi: 10.1016/j.geomorph.2015.02.033

Iverson, R. M., Logan, M., LaHusen, R. G., & Berti, M. (2010). The perfect debris flow? aggregated results from 28 large-scale experiments. *Journal of Geophysical Research*, *115*(F3). doi: 10.1029/2009jf001514

Jenkins, J. T. (2007). Dense inclined flows of inelastic spheres. *Granular Matter*, *10*(1), 47–52. doi: 10.1007/s10035-007-0057-z

Jenkins, J. T., & Savage, S. B. (1983). A theory for the rapid flow of identical, smooth, nearly elastic, spherical particles. *Journal of Fluid Mechanics*, *130*(-1), 187. doi: 10.1017/s0022112083001044

Kaitna, R., Dietrich, W. E., & Hsu, L. (2014). Surface slopes, velocity profiles and fluid pressure in coarse-grained debris flows saturated with water and mud. *Journal of Fluid Mechanics*, *741*, 377–403. doi: 10.1017/jfm.2013.675

Kaitna, R., Palucis, M. C., Yohannes, B., Hill, K. M., & Dietrich, W. E. (2016). Effects of coarse grain size distribution and fine particle content on pore fluid pressure and shear behavior in experimental debris flows. *Journal of Geophysical Research: Earth Surface*, *121*(2), 415–441. doi: 10.1002/2015jf003725

Kesseler, M., Heller, V., & Turnbull, B. (2020). Grain Reynolds Number scale effects in dry granular slides. *Journal of Geophysical Research: Earth Surface*, *125*(1). doi: 10.1029/2019jf005347

Lanzoni, S., Gregoretti, C., & Stancanelli, L. M. (2017). Coarse-grained debris flow dynamics on erodible beds. *Journal of Geophysical Research: Earth Surface*, *122*(3), 592–614. doi: 10.1002/2016jf004046

Legros, F. (2002). The mobility of long-runout landslides. *Engineering Geology*, *63*(3-4), 301–331. doi: 10.1016/s0013-7952(01)00090-4

Leonardi, A., Cabrera, M., Wittel, F. K., Kaitna, R., Mendoza, M., Wu, W., & Herrmann, H. J. (2015). Granular-front formation in free-surface flow of concentrated suspensions. *Physical Review E*, *92*(5). doi: 10.1103/physreve.92.052204

Lun, C. K. K. (1991). Kinetic theory for granular flow of dense, slightly inelastic, slightly rough spheres. *Journal of Fluid Mechanics*, *233*, 539–559. doi: 10.1017/s0022112091000599

Lun, C. K. K., & Savage, S. B. (1986). The effects of an impact velocity dependent coefficient of restitution on stresses developed by sheared granular materials. *Acta Mechanica*, *63*(1-4), 15–44. doi: 10.1007/bf01182538

Mangeney, A., Roche, O., Hungr, O., Mangold, N., Faccanoni, G., & Lucas, A. (2010). Erosion and mobility in granular collapse over sloping beds. *Journal of Geophysical Research*, *115*(F3). doi: 10.1029/2009jf001462

McArdell, B. W., Bartelt, P., & Kowalski, J. (2007). Field observations of basal forces and fluid pore pressure in a debris flow. *Geophysical Research Letters*, *34*(7). doi: 10.1029/2006gl029183

McDougall, S. (2017). 2014 canadian geotechnical colloquium: Landslide runout analysis — current practice and challenges. *Canadian Geotechnical Journal*, *54*(5), 605–620. doi: 10.1139/cgj-2016-0104

Nagl, G., Hübl, J., & Kaitna, R. (2020). Velocity profiles and basal stresses in natural debris flows. *Earth Surface Processes and Landforms*, *45*(8), 1764–1776. doi: 10.1002/esp.4844

Parez, S., & Aharonov, E. (2015). Long runout landslides: a solution from granular mechanics. *Frontiers in Physics*, *3*. doi: 10.3389/fphy.2015.00080

Pastor, M., Blanc, T., Haddad, B., Drempetic, V., Morles, M. S., Dutto, P., ... Merodo, J. A. F. (2014). Depth averaged models for fast landslide propagation: Mathematical, rheological and numerical aspects. *Archives of Computational Methods in Engineering*, *22*(1), 67–104. doi: 10.1007/s11831-014-9110-3

Pudasaini, S. P., Wang, Y., & Hutter, K. (2005). Modelling debris flows down general channels. *Natural Hazards and Earth System Sciences*, *5*(6), 799–819. doi: 10.5194/nhess-5-799-2005

Raymond, G. P. (2002). Reinforced ballast behaviour subjected to repeated load. *Geotextiles and Geomembranes*, *20*(1), 39–61. doi: 10.1016/s0266-1144(01)00024-3

Rickenmann, D. (2011). Runout prediction methods. In O. Hungr & M. Jakob (Eds.), *Debris-flow hazards and related phenomena* (pp. 305–324). Springer Berlin Heidelberg.

Schlunegger, F., Badoux, A., McArdell, B. W., Gwerder, C., Schnydrig, D., Rieke-Zapp, D., & Molnar, P. (2009). Limits of sediment transfer in an alpine debris-flow catchment, illgraben, switzerland. *Quaternary Science Reviews*, *28*(11-12), 1097–1105. doi: 10.1016/j.quascirev.2008.10.025

Shugar, D. H., Jacquemart, M., Shean, D., Bhushan, S., Upadhyay, K., Sattar, A., ... Westoby, M. J. (2021). A massive rock and ice avalanche caused the 2021 disaster at chamoli, indian himalaya. *Science*, *373*(6552), 300-306. Retrieved from `https://www.science.org/doi/abs/10.1126/science.abh4455` doi: 10.1126/science.abh4455

Staron, L., & Lajeunesse, E. (2009). Understanding how volume affects the mobility of dry debris flows. *Geophysical Research Letters*, *36*(12). doi: 10.1029/2009gl038229

Taylor-Noonan, A. M., Gollin, D., Bowman, E. T., & Take, W. A. (2021). The influence of image analysis methodology on the calculation of granular temperature for granular flows. *Granular Matter*, *23*(4). doi: 10.1007/s10035-021-01153-y

Tayyebi, S. M., Pastor, M., & Stickle, M. M. (2021). Two-phase SPH numerical study of pore-water pressure effect on debris flows mobility: Yu Tung debris flow. *Computers and Geotechnics*, *132*, 103973. doi: 10.1016/j.compgeo.2020.103973

Tsubaki, T., Hashimoto, H., & Suetsugi, T. (1983). Interparticle stresses and characteristics of debris flow. *Journal of Hydroscience and Hydraulic Engineering*, *1*(2), 67–82.

Turnbull, B., Bowman, E. T., & McElwaine, J. N. (2015). Debris flows: Experiments and modelling. *Comptes Rendus Physique*, *16*(1), 86–96. doi: 10.1016/j.crhy.2014.11.006

Voight, B., & Faust, C. (1982). Frictional heat and strength loss in some rapid landslides. *Géotechnique*, *32*(1), 43–54. doi: 10.1680/geot.1982.32.1.43

Walter, F., Amann, F., Kos, A., Kenner, R., Phillips, M., de Preux, A., ... Bonanomi, Y. (2020). Direct observations of a three million cubic meter rock-slope collapse with almost immediate initiation of ensuing debris flows. *Geomorphology*, *351*, 106933. doi: 10.1016/j.geomorph.2019.106933

Zhou, G. G. D., Li, S., Song, D., Choi, C. E., & Chen, X. (2018). Depositional mechanisms and morphology of debris flow: physical modelling. *Landslides*, *16*(2), 315–332. doi: 10.1007/s10346-018-1095-9

Figure 1.

(**a**) definitions of landslide geometry statistics

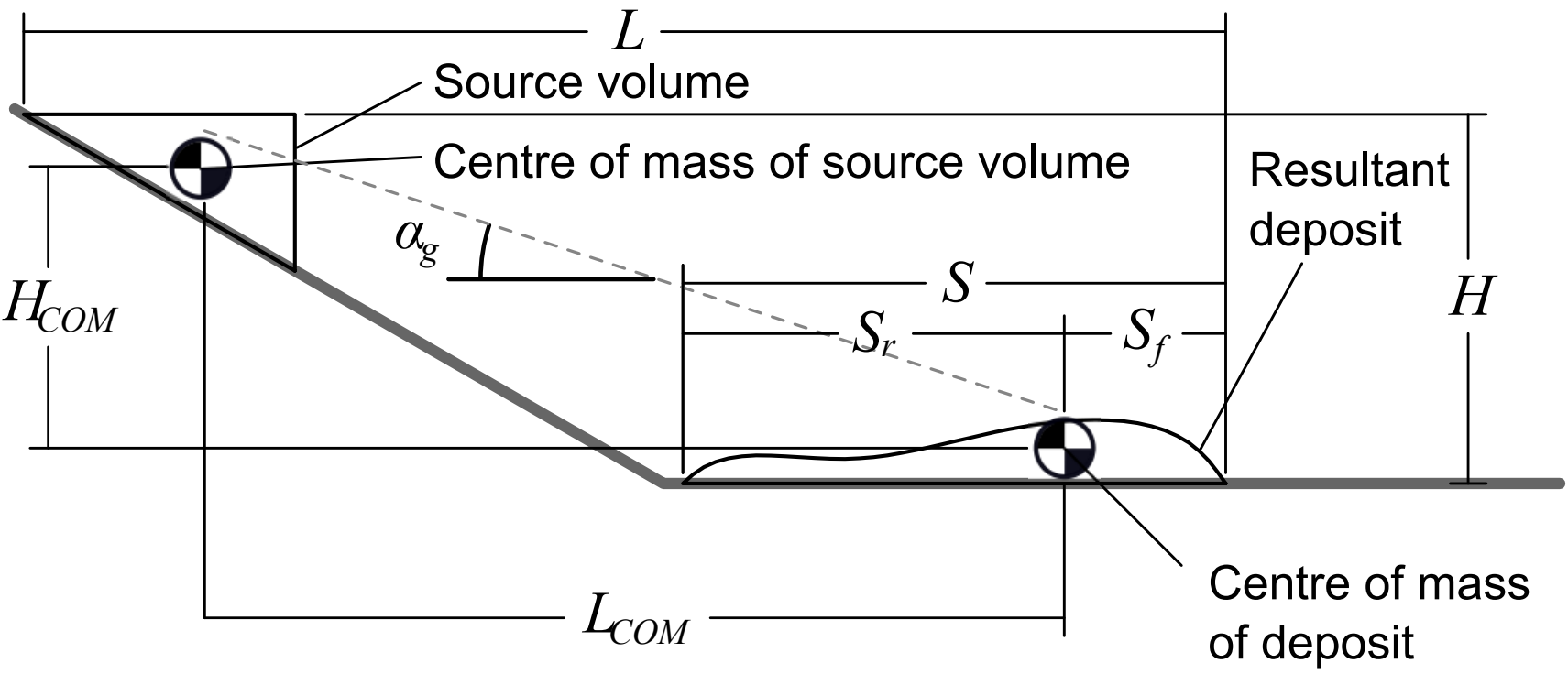

(**b**) travel angle invariant with source volume

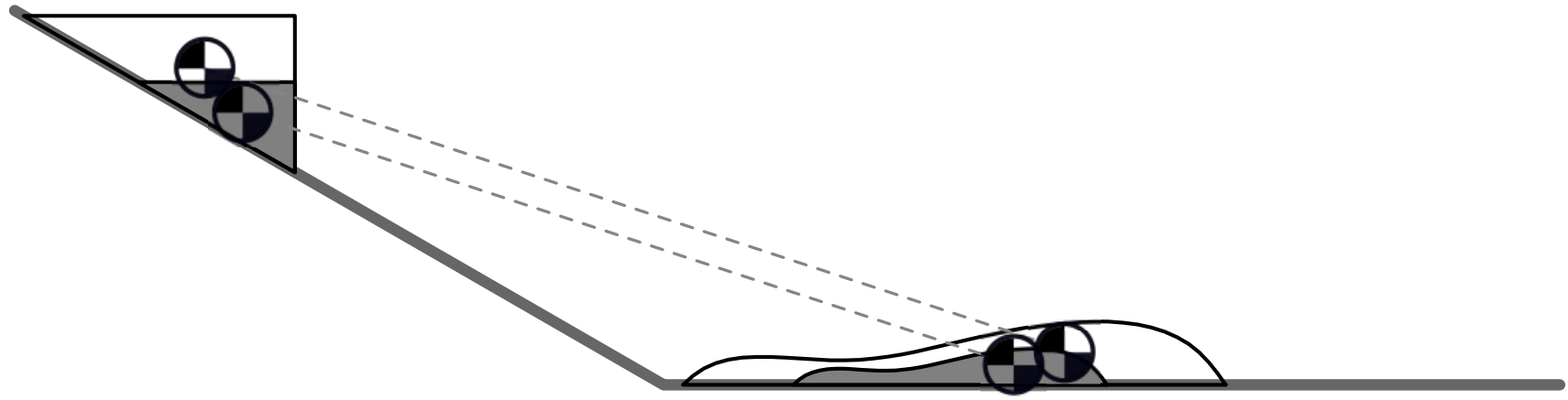

(**c**) travel angle variant with source volume

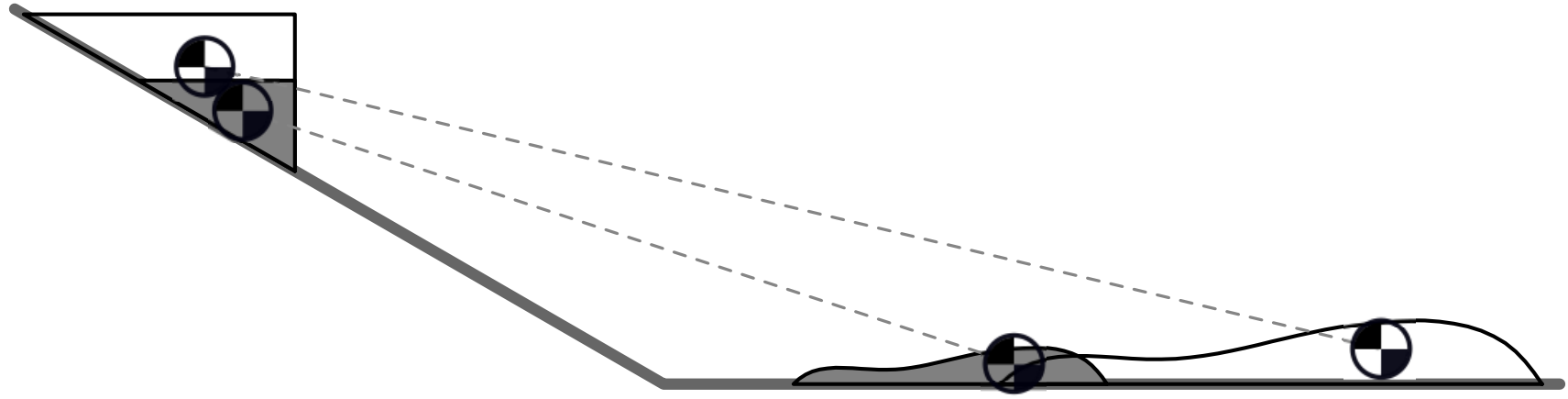

Figure 2.

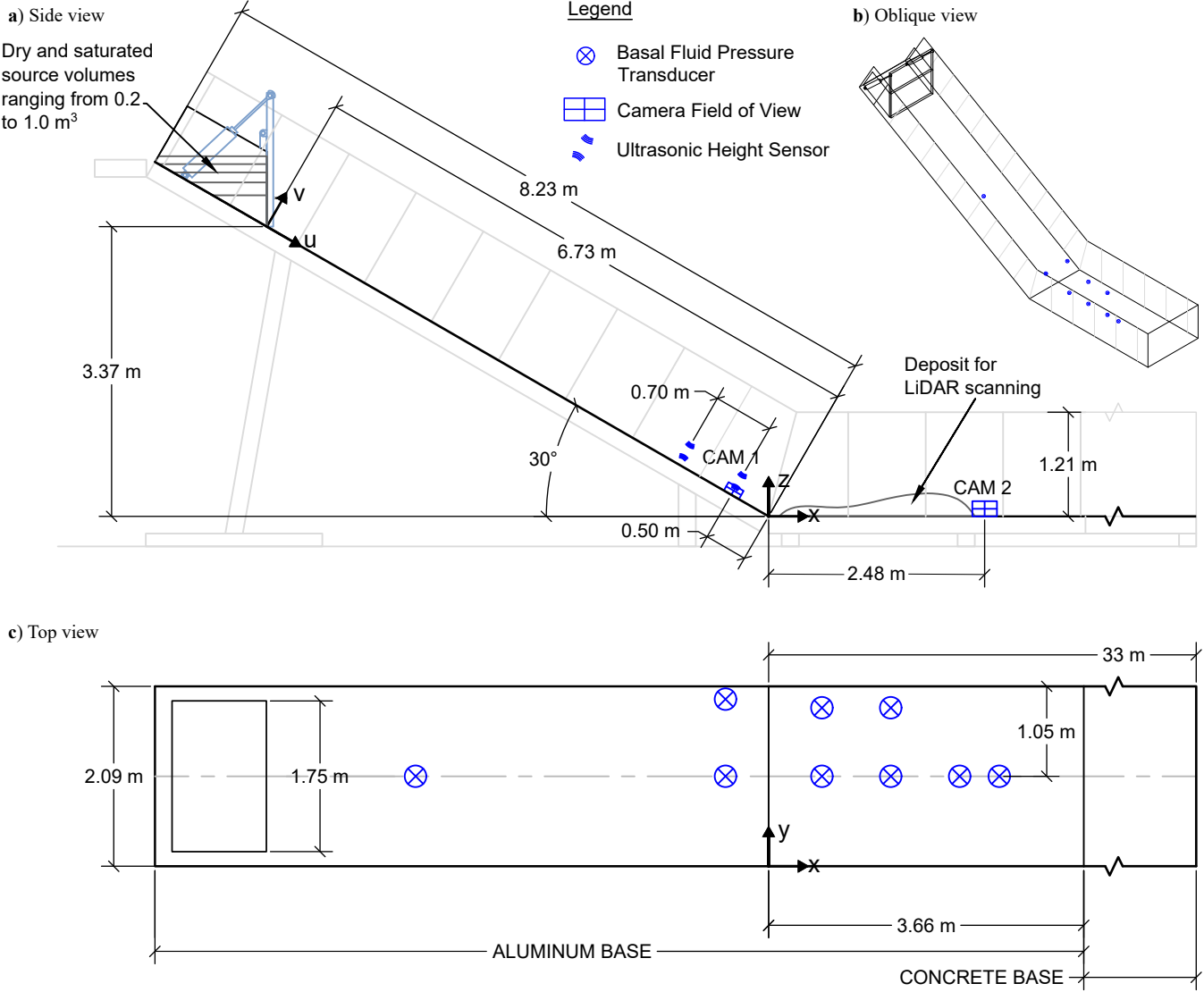
a) Side view
Dry and saturated source volumes ranging from 0.2 to 1.0 m3
Legend
Basal Fluid Pressure Transducer
Camera Field of View
Ultrasonic Height Sensor
b) Oblique view
8.23 m
6.73 m
v
u
3.37 m
30°
0.70 m
CAM 1
Deposit for LiDAR scanning
CAM 2
1.21 m
z
x
0.50 m
2.48 m
c) Top view
33 m
1.05 m
2.09 m
1.75 m
y
x
3.66 m
ALUMINUM BASE
CONCRETE BASE

Figure 3.

(a) Particle tracking vectors

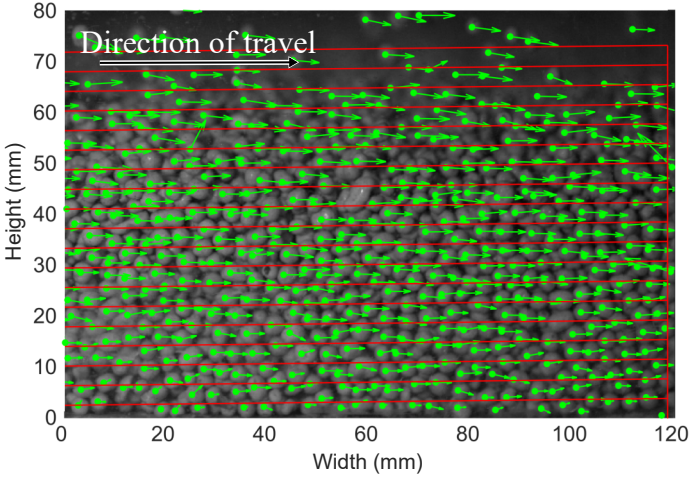

(b) velocity profile

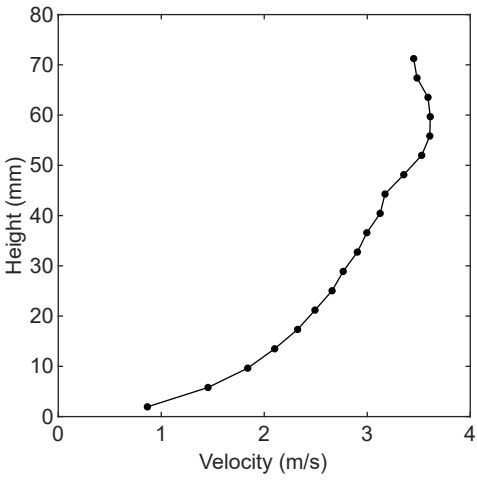

(c) High-speed video with Voronoï polygons drawn

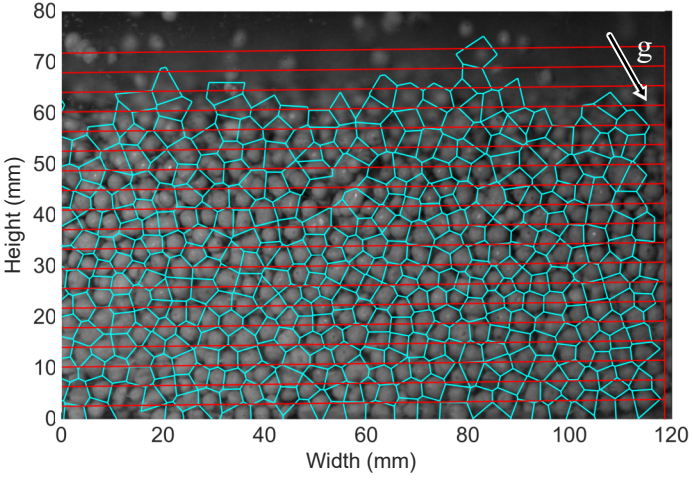

(d) volume fraction profile

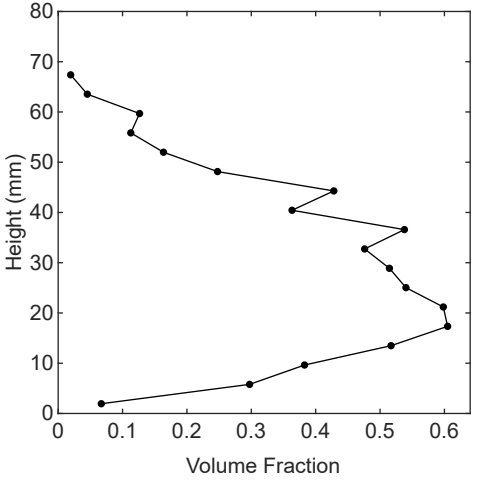

Figure 4.

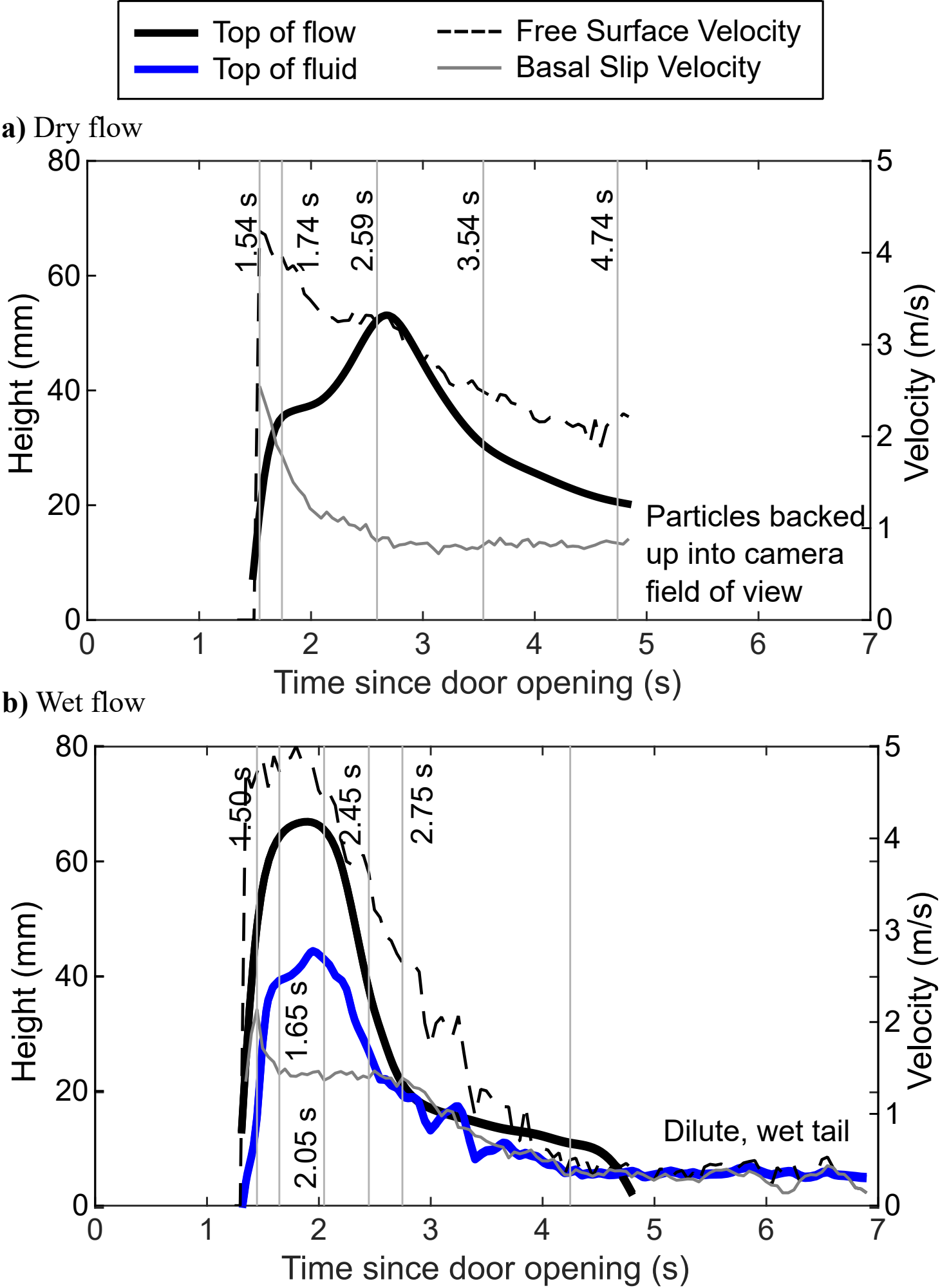
Top of flow
Top of fluid
Free Surface Velocity
Basal Slip Velocity
a) Dry flow
1.54 s
1.74 s
2.59 s
3.54 s
4.74 s
Particles backed up into camera field of view
Height (mm)
Velocity (m/s)
Time since door opening (s)
b) Wet flow
1.50 s
2.45 s
2.75 s
1.65 s
2.05 s
Dilute, wet tail
Height (mm)
Velocity (m/s)
Time since door opening (s)

Figure 5.

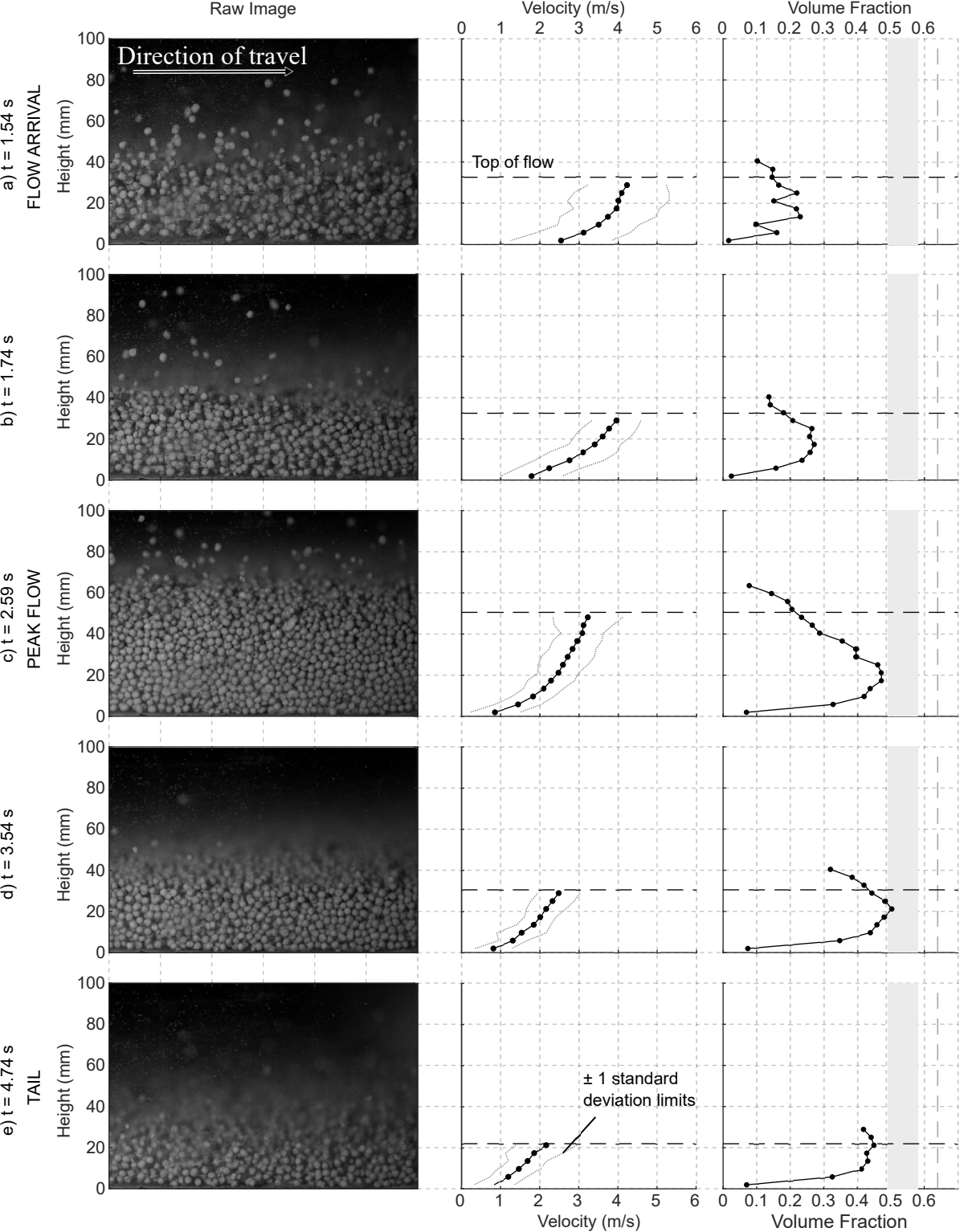
Raw Image
Velocity (m/s)
Volume Fraction
Direction of travel
Height (mm)
a) t = 1.54 s
FLOW ARRIVAL
Top of flow
b) t = 1.74 s
c) t = 2.59 s
PEAK FLOW
d) t = 3.54 s
e) t = 4.74 s
TAIL
± 1 standard
deviation limits
0 1 2 3 4 5 6
0 0.1 0.2 0.3 0.4 0.5 0.6
0 20 40 60 80 100

Figure 6.

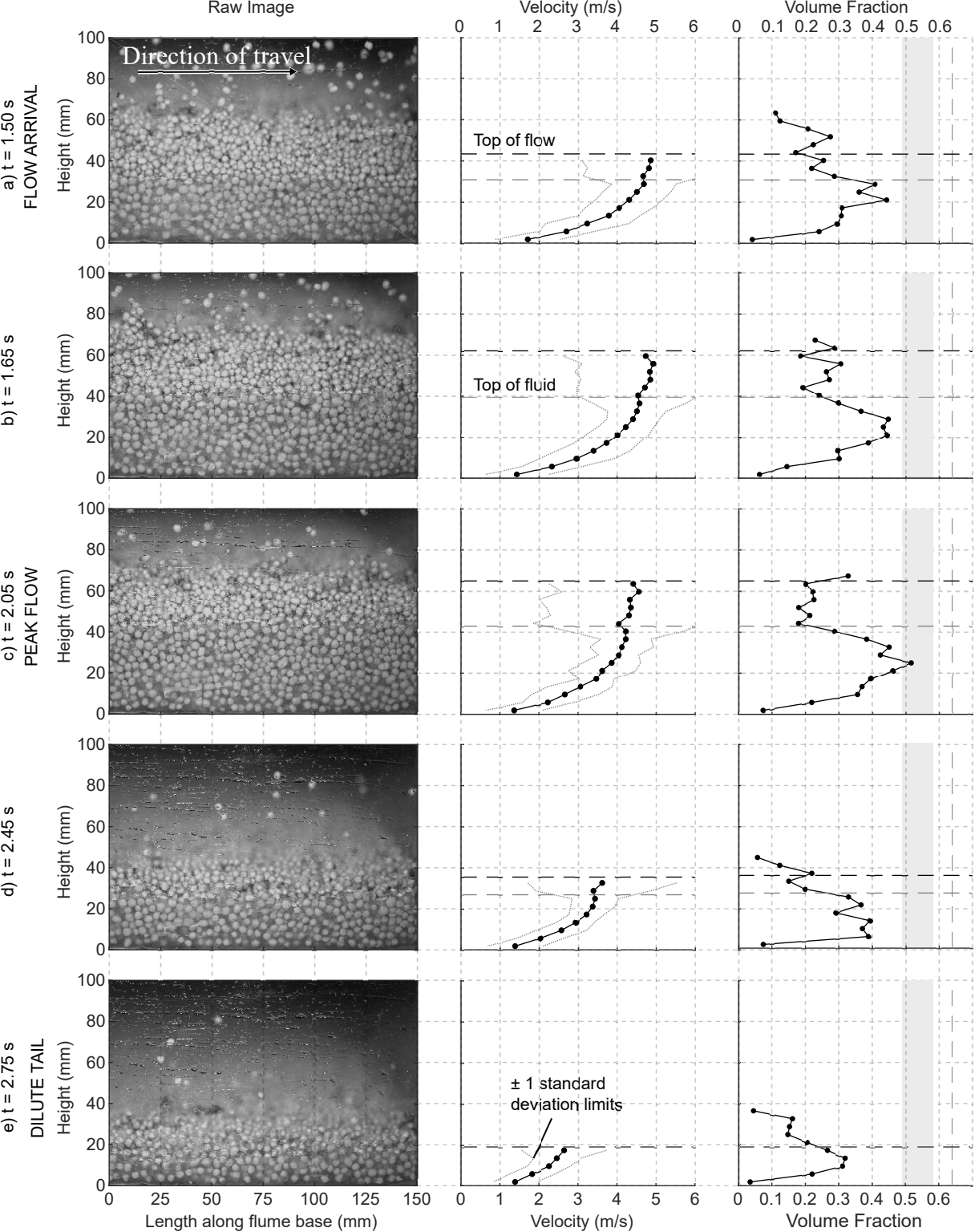
Raw Image
Velocity (m/s)
Volume Fraction
Direction of travel
Top of flow
Top of fluid
± 1 standard deviation limits
a) t = 1.50 s FLOW ARRIVAL
b) t = 1.65 s
c) t = 2.05 s PEAK FLOW
d) t = 2.45 s
e) t = 2.75 s DILUTE TAIL
Height (mm)
Length along flume base (mm)
Velocity (m/s)
Volume Fraction

Figure 7.

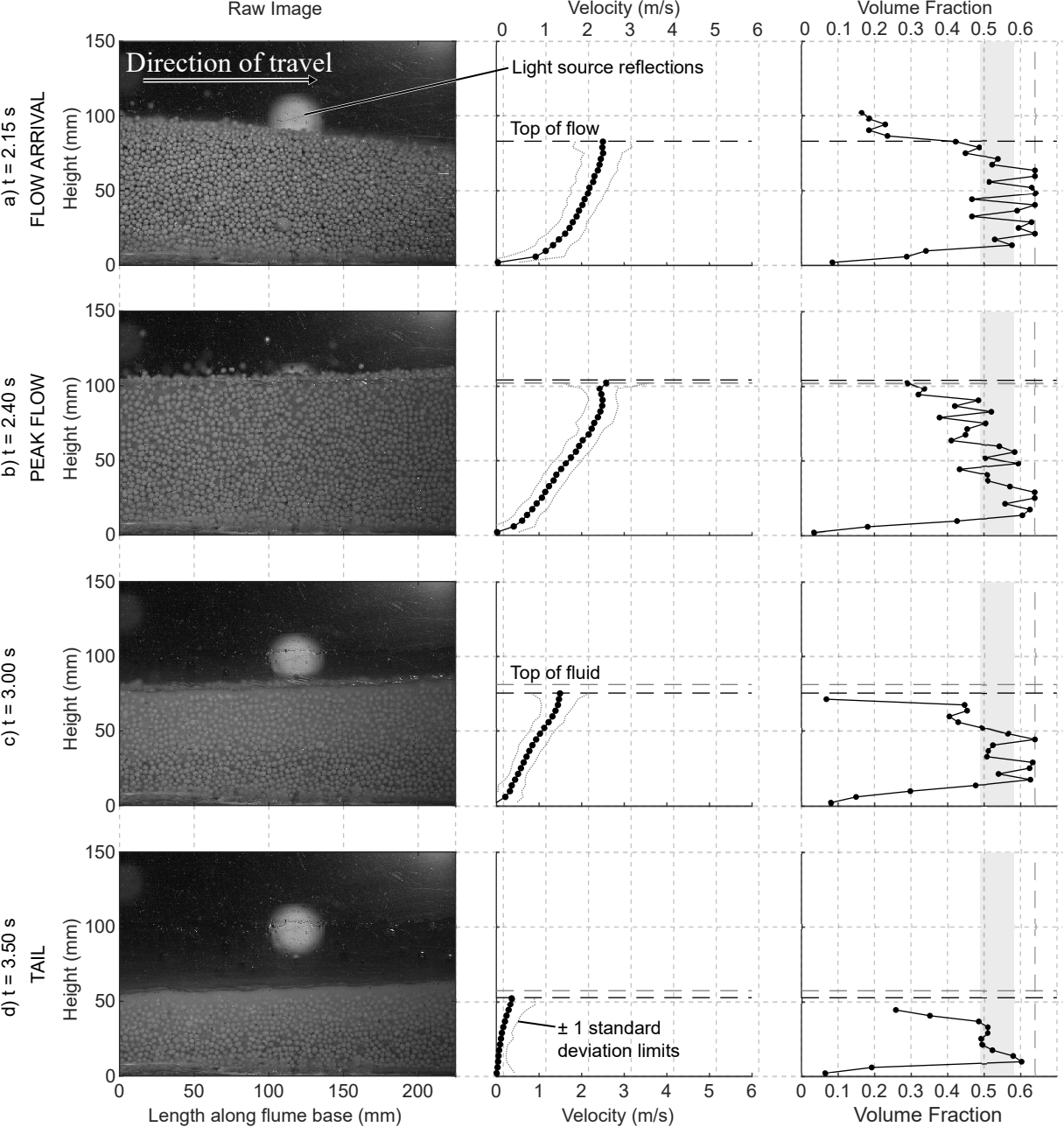
Raw Image
Velocity (m/s)
Volume Fraction
Direction of travel
Light source reflections
Top of flow
Top of fluid
± 1 standard deviation limits
a) t = 2.15 s FLOW ARRIVAL
b) t = 2.40 s PEAK FLOW
c) t = 3.00 s
d) t = 3.50 s TAIL
Height (mm)
Length along flume base (mm)
Velocity (m/s)
Volume Fraction

Figure 8.

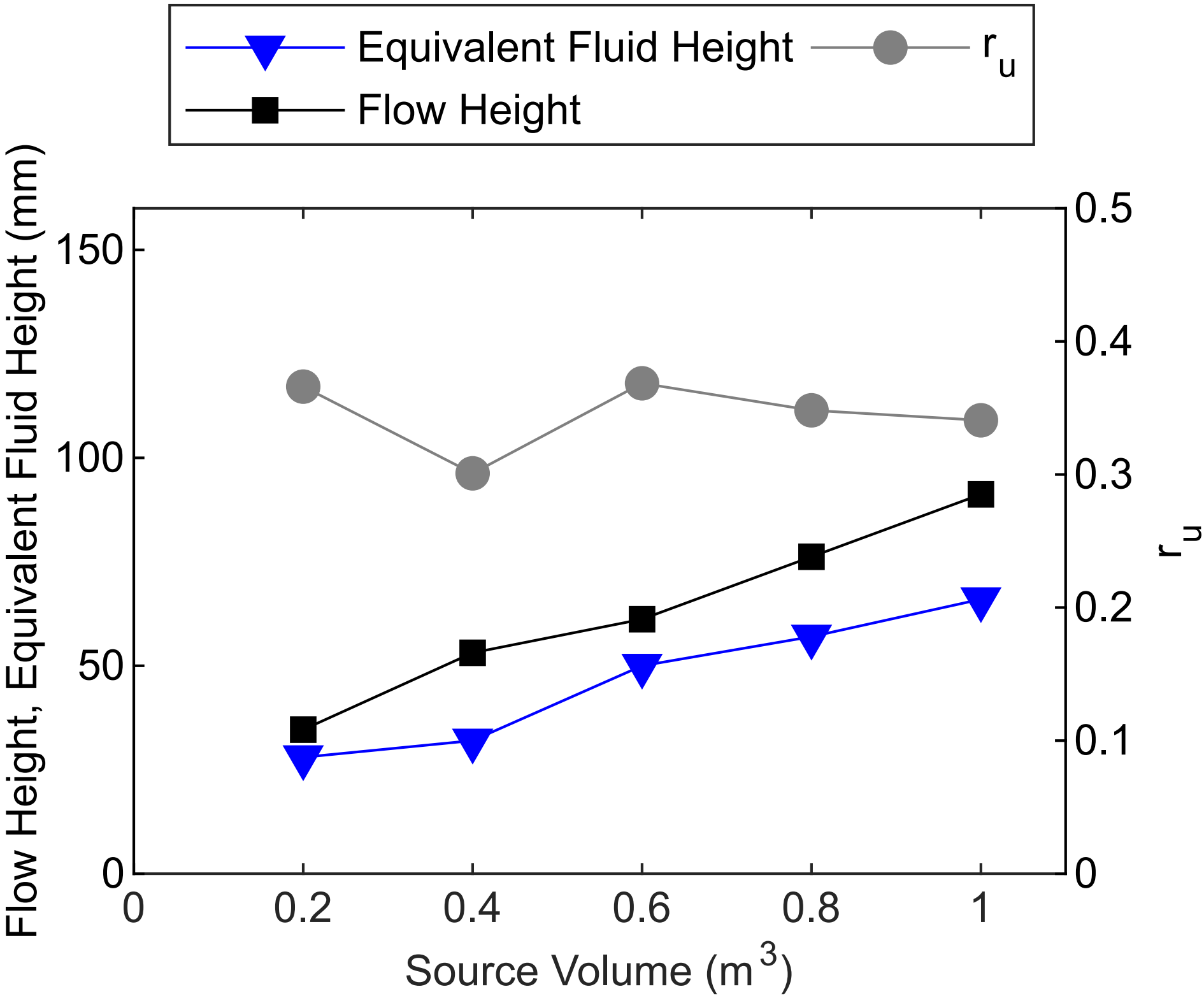
Equivalent Fluid Height
r_u
Flow Height
Flow Height, Equivalent Fluid Height (mm)
150
100
50
0
0.5
0.4
0.3
0.2
0.1
0
r_u
0
0.2
0.4
0.6
0.8
1
Source Volume (m^3)

Figure 9.

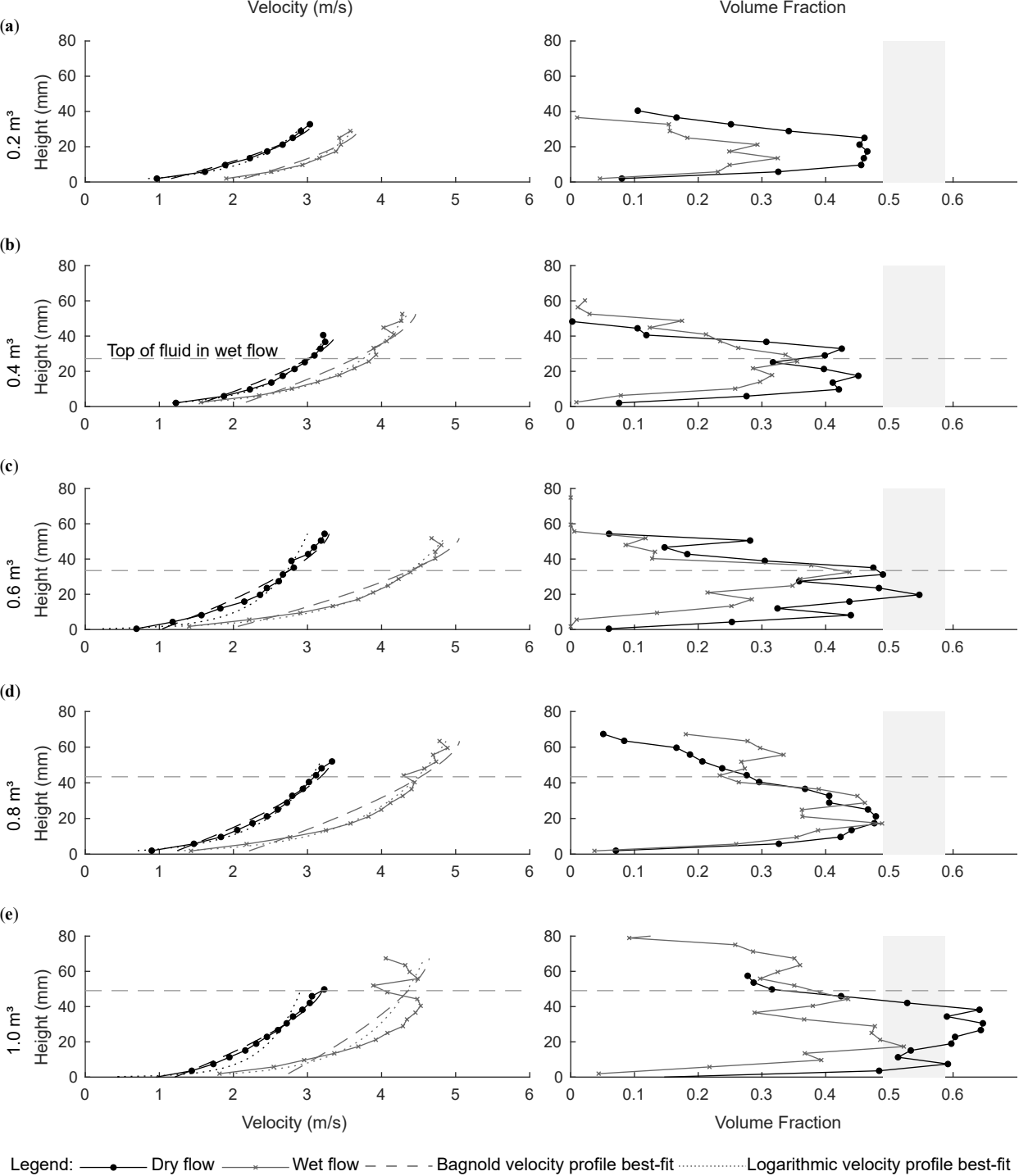
Velocity (m/s)
Volume Fraction
(a)
(b)
(c)
(d)
(e)
0.2 m³
0.4 m³
0.6 m³
0.8 m³
1.0 m³
Height (mm)
Top of fluid in wet flow
Velocity (m/s)
Volume Fraction
Legend: Dry flow Wet flow Bagnold velocity profile best-fit Logarithmic velocity profile best-fit

Figure 10.

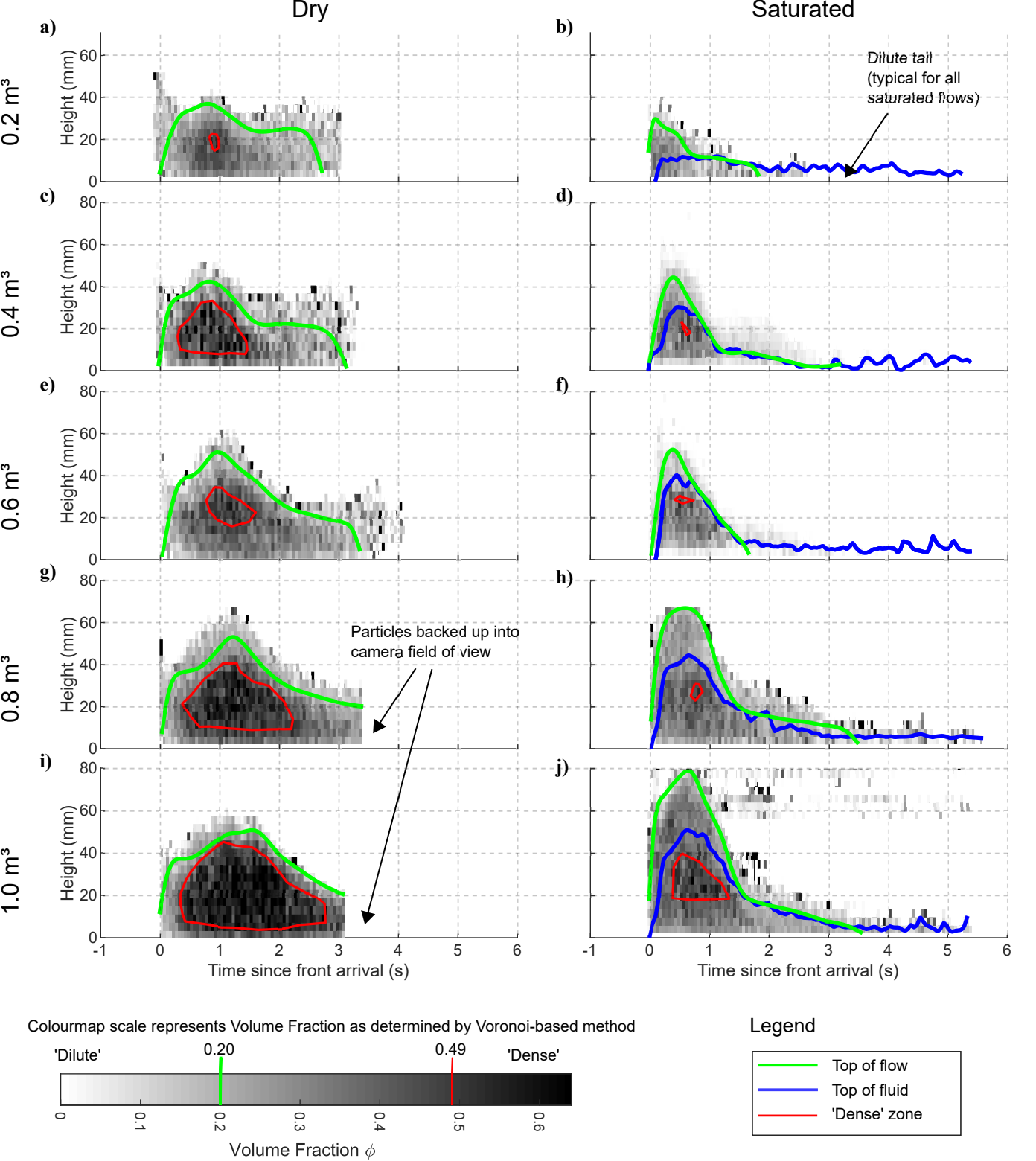
Dry
Saturated
a)
b)
c)
d)
e)
f)
g)
h)
i)
j)
0.2 m³
0.4 m³
0.6 m³
0.8 m³
1.0 m³
Height (mm)
Dilute tail
(typical for all
saturated flows)
Particles backed up into
camera field of view
Time since front arrival (s)
Colourmap scale represents Volume Fraction as determined by Voronoi-based method
'Dilute'
0.20
0.49
'Dense'
Volume Fraction ϕ
Legend
Top of flow
Top of fluid
'Dense' zone

Figure 11.

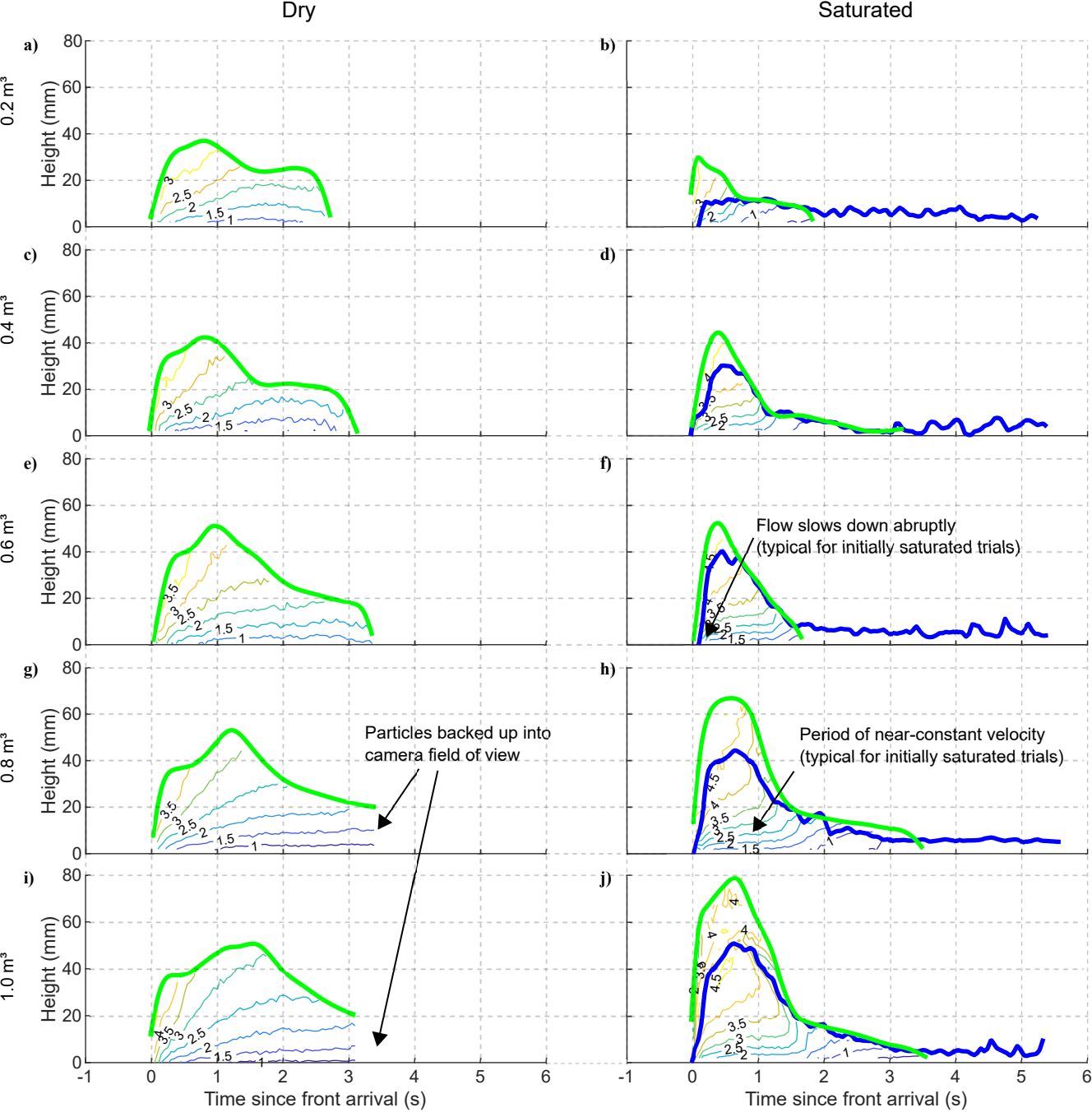
Dry
Saturated
a)
b)
c)
d)
e)
f)
g)
h)
i)
j)
0.2 m³
0.4 m³
0.6 m³
0.8 m³
1.0 m³
Height (mm)
Time since front arrival (s)
Flow slows down abruptly
(typical for initially saturated trials)
Particles backed up into
camera field of view
Period of near-constant velocity
(typical for initially saturated trials)
Contour lines represent streamwise flow velocity
as determined by PTV method
Legend
Top of flow
Top of fluid

Figure 12.

a) Dry

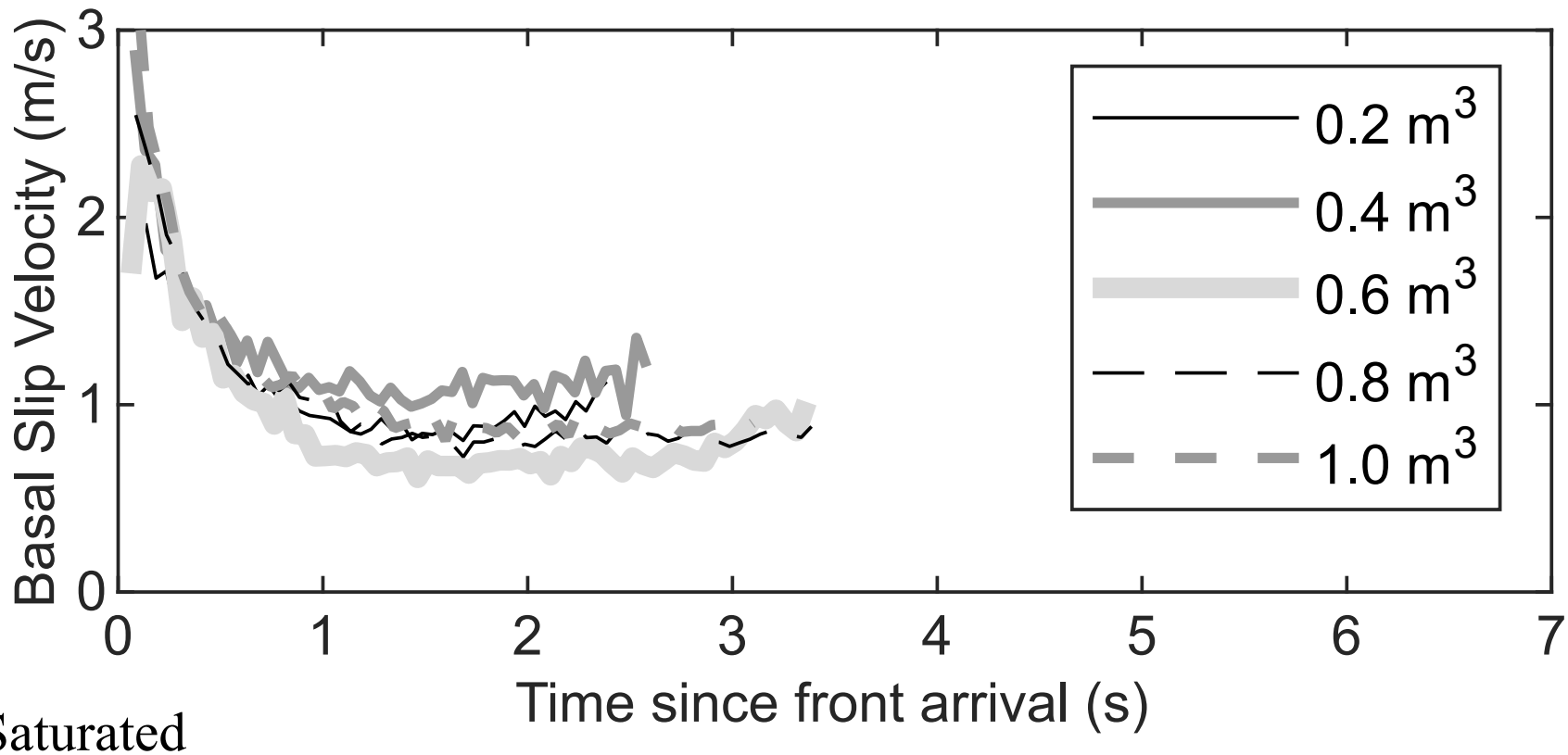

b) Saturated

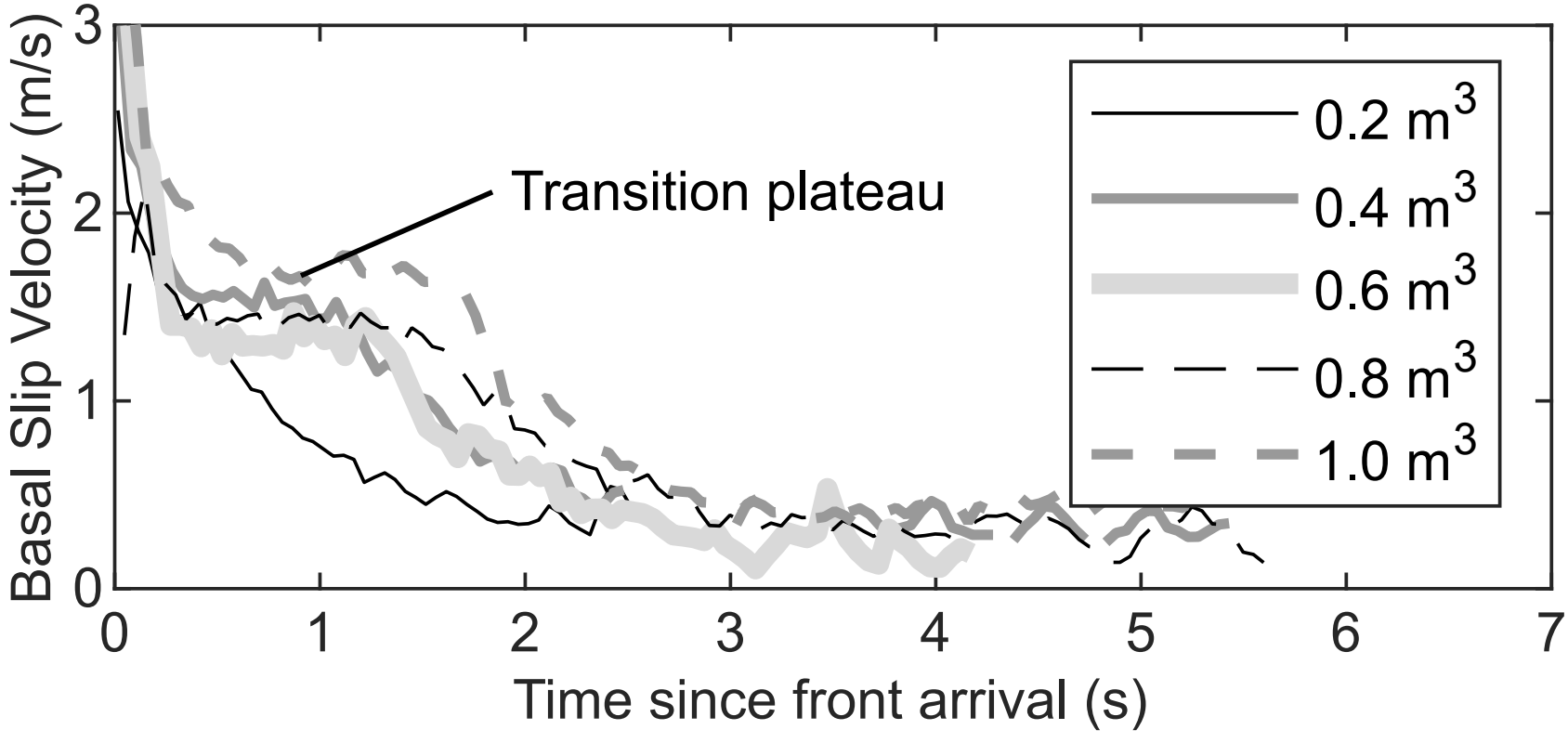

Figure 13.

(**a**) Dry trials

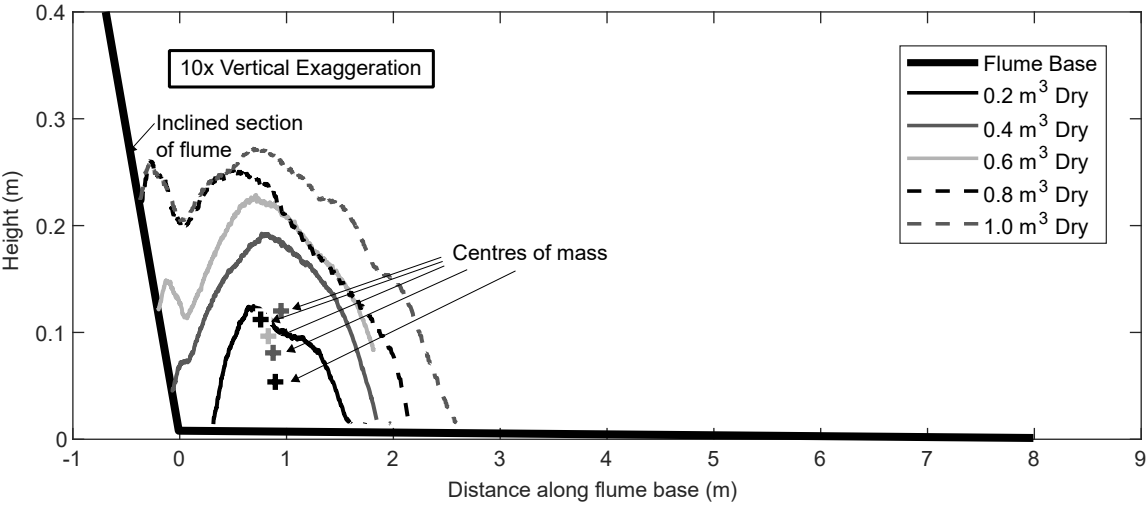

(**b**) Initially saturated trials

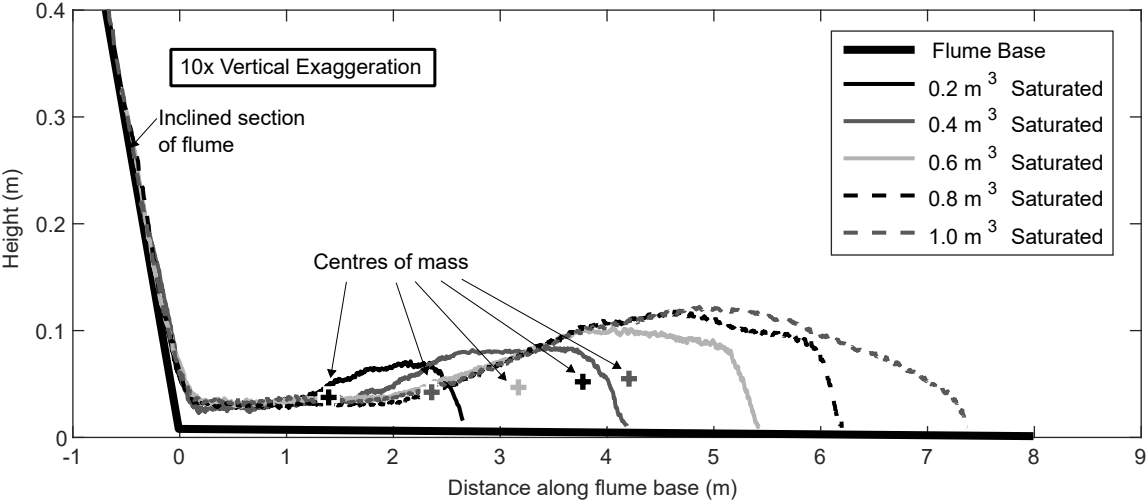

Figure 14.

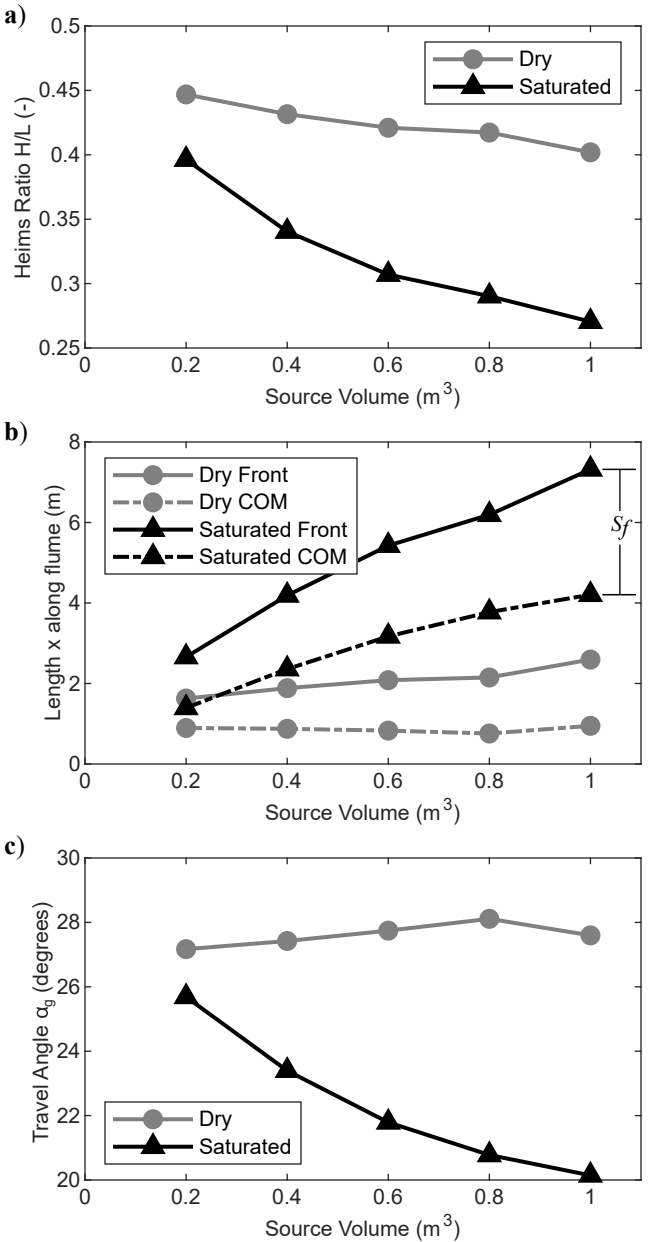
a)
Heims Ratio H/L (-)
0.5
0.45
0.4
0.35
0.3
0.25
0
0.2
0.4
0.6
0.8
1
Source Volume (m3)
Dry
Saturated
b)
Length x along flume (m)
8
6
4
2
0
Dry Front
Dry COM
Saturated Front
Saturated COM
Sf
Source Volume (m3)
c)
Travel Angle αg (degrees)
30
28
26
24
22
20
Dry
Saturated
Source Volume (m3)